iScience

Article

Synthesis of versatile neuromodulatory molecules by a gut microbial glutamate decarboxylase

Graphical abstract

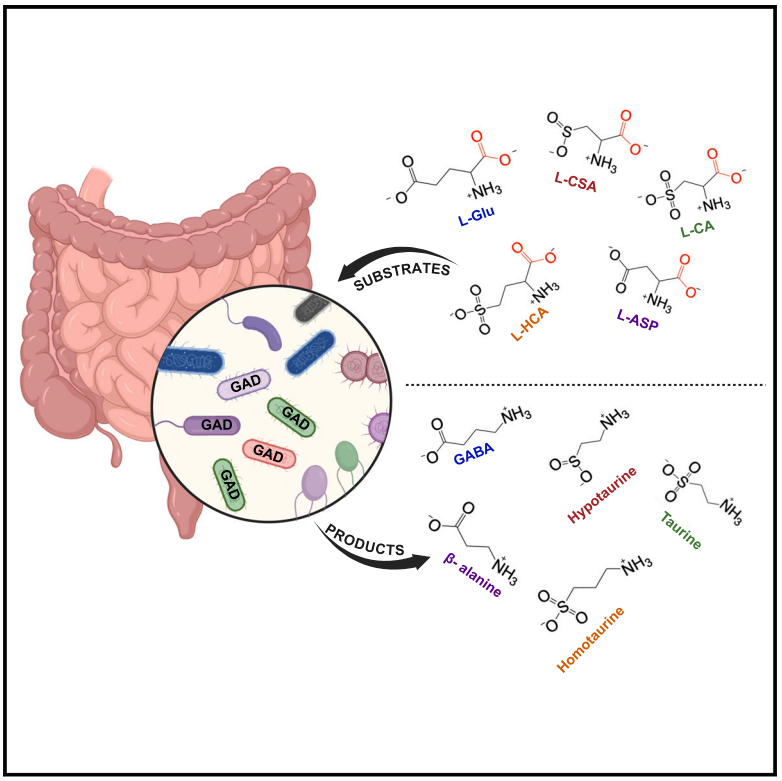

Highlights

- Glutamate decarboxylase from *B. fragilis* produces multiple neuromodulatory molecules
- Evolving *Bf*GAD doubled its taurine production
- Engineered *Bf*GAD variants exhibit structural and catalytic perturbations

Authors

Pavani Dadi, Clint W. Pauling, Abhishek Shrivastava, Dhara D. Shah

Correspondence

dhara.shah1@asu.edu

In brief

Biochemistry; Molecular neuroscience; Microbiology

Dadi et al., 2025, iScience *28*, 112289
April 18, 2025
https://doi.org/10.1016/j.isci.2025.112289

CellPress

iScience

CellPress
OPEN ACCESS

Article

Synthesis of versatile neuromodulatory molecules by a gut microbial glutamate decarboxylase

Pavani Dadi,[1,2] Clint W. Pauling,[1,3] Abhishek Shrivastava,[1,2] and Dhara D. Shah[1,3,4,*]
[1]Biodesign Center for Fundamental and Applied Microbiomics, Arizona State University, Tempe, AZ 85281, USA
[2]School of Life Sciences, Arizona State University, Tempe, AZ 85281, USA
[3]School of Mathematical and Natural Sciences, Arizona State University, Glendale, AZ 85306, USA
[4]Lead contact
*Correspondence: dhara.shah1@asu.edu
https://doi.org/10.1016/j.isci.2025.112289

SUMMARY

Dysbiosis of the microbiome correlates with many neurological disorders, yet very little is known about the chemistry that controls the production of neuromodulatory molecules by gut microbes. Here, we found that an enzyme glutamate decarboxylase (*Bf*GAD) of a gut microbe *Bacteroides fragilis* forms multiple neuromodulatory molecules such as γ-aminobutyric acid (GABA), hypotaurine, taurine, homotaurine, and β-alanine. We evolved *Bf*GAD and doubled its taurine productivity. Additionally, we increased its specificity toward the substrate L-glutamate. Here, we provide a chemical strategy via which the *Bf*GAD activity could be fine-tuned. In future, this strategy could be used to modulate the production of neuromodulatory molecules by gut microbes.

INTRODUCTION

Low levels of inhibitory neurotransmitter like γ-aminobutyric acid (GABA) have been associated with neurological disorders such as epilepsy, schizophrenia, autism spectrum disorder (ASD), attention deficit hyperactivity disorder (ADHD), panic disorder, post-traumatic stress disorder (PTSD), major depressive disorder, progressive multiple sclerosis, dementia, and Alzheimer's disease.[1–12] Taurine, another amino acid abundant in the brain,[13] acts as a $GABA_A$ receptor agonist and exerts downstream effects similar to GABA.[14] Taurine concentrations are altered in individuals with Alzheimer's disease, with reduced levels observed in the brain[15–21], increased urinary excretion of taurine is found in elderly dementia patients,[22] and lower fecal levels of GABA and taurine were found in gnotobiotic mice transplanted with fecal microbiota from an Alzheimer's patient.[23] Based on these observations, supplementation with taurine and its analogs has been investigated in Alzheimer's disease models.[24,25] In one such study, homotaurine, a molecule similar to taurine, restored cognitive functions in patients with Alzheimer's disease.[26] In addition, it was also observed that taurine reverses cognitive deficits in APP/PS1 mouse model[25] and improves learning and memory in mice.[24,27]

Studies linking gut microbial dysbiosis to dementia and Alzheimer's disease frequently report changes in the abundance of *Bacteroides* sp.,[28–33] which are key members of the human gut microbiome[34,35] and can produce GABA[36,37] (Figure 1A). Most *Bacteroides* species encode glutamate decarboxylase (GAD), a pyridoxal phosphate (PLP)-dependent enzyme that converts the excitatory neurotransmitter glutamate into the inhibitory neurotransmitter GABA.[38] Applications of enzymatic engineering to enhance the substrate specificity and efficiency of GADs from abundant *Bacteroides* sp. in the gut microbiome could offer a potential therapy for neurodegenerative disorders. However, the chemistry through which GADs from any *Bacteroides* species produce GABA remains largely unknown. In this study, we investigated, evolved, and optimized GAD from the human gut microbe *Bacteroides fragilis* (*Bf*GAD) to produce various neuromodulatory molecules, including GABA, taurine, its analogs, and β-alanine. Biochemical characterization revealed that *Bf*GAD exhibits distinct kinetic and functional properties compared to other known prokaryotic GADs. We found that, while *Bf*GAD prefers L-glutamate, it can also decarboxylate other substrates to produce multiple neuromodulatory molecules. This versatility suggests that *Bf*GAD may play a critical role in complex systems with diverse substrates, a trait advantageous for microbes in the mammalian gut. Using rational protein engineering, we enhanced *Bf*GAD to produce twice as much taurine as the native enzyme and improved its specificity for L-glutamate. We demonstrate that *Bf*GAD is highly amenable to enzymatic engineering, even tolerating modifications to its active site. Our study lays the foundation for the rational design and engineering of *Bf*GAD, which could, in the future, enable the development of gut microbes capable of producing diverse neuromodulatory compounds.

RESULTS AND DISCUSSION

GADs are prevalent in the *Bacteroides* genus

Prior research has implicated gut microbial contributions to the production of GABA, specifically from the *Bacteroides* genus.[36,37] GABA, a neurotransmitter, is modulated in many neurodegenerative diseases, including Alzheimer's and dementia, where lower GABA levels have been consistently reported.[12] Microbes from

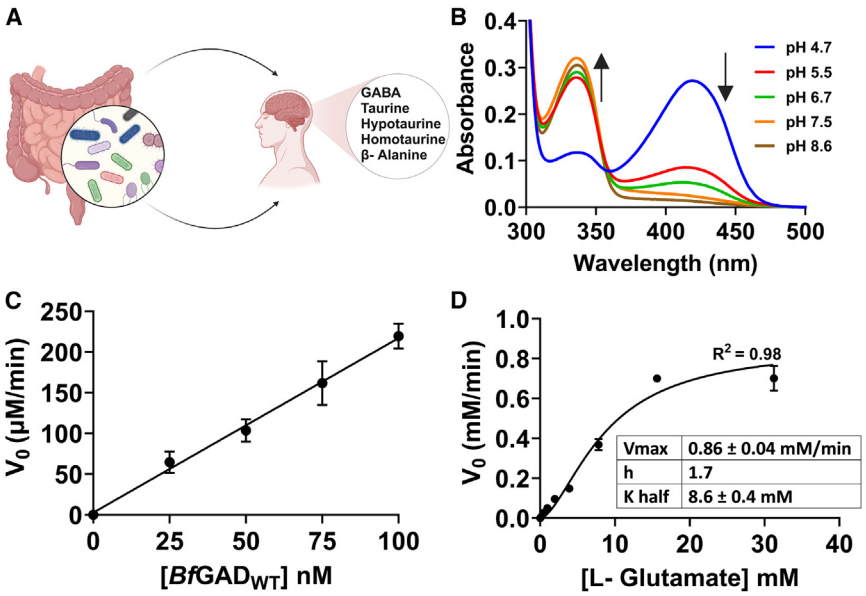

Figure 1. Characterization of *Bf*GAD$_{WT}$

(A) Possible role of gut microbes in producing neuromodulatory molecules.

(B) Spectra of PLP cofactor bound to the holoenzyme *Bf*GAD$_{WT}$ captured at various pH, depicting tautomers of internal aldimine at 335 and 420 nm.

(C) Plot of initial velocity as a function of *Bf*GAD$_{WT}$ concentrations (n = 4). Error bars represent SD.

(D) Plot of initial velocity vs. L-glutamate concentrations (n = 2). Error bars represent SD. The solid line is a sigmoidal fit to the data.

the genus *Bacteroides* are known to be fluctuated in individuals afflicted by Alzheimer's and dementia.[30–33] Due to the prevalent nature of *Bacteroides* in the gut and the modulation of *Bacteroides* during Alzheimer's, we explored the mechanism by which GABA is produced in these organisms.

A bioinformatics analysis showed that many species of the *Bacteroides* genus harbor genes annotated as GAD (Figure S1). Multiple sequence alignment performed with GADs from various species of the genus *Bacteroides* displays a high (>90%) sequence similarity (Figure S1), and a GAD, herein referred as *Bf*GAD, from the model organism *B. fragilis* was selected as a candidate enzyme representing annotated GADs in all *Bacteroides* (Figure S2). Additional multiple sequence alignment performed with gut microbial GADs including *Bf*GAD revealed that many catalytic residues, predicted to be involved in either substrate binding (highlighted in cyan) or cofactor (PLP) binding (highlighted in yellow), are highly conserved (Figure S3),[39,40] and GADs from gut microbes such as *Alistipes putredinis* and *Parabacteroides merdae* are most closely related to *Bf*GAD (Figure S4).

Wild-type *Bf*GAD forms an oligomer

The recombinant wild-type *Bf*GAD (*Bf*GAD$_{WT}$) with an N-terminal His-tag was purified using Ni-NTA affinity chromatography. SDS-PAGE analysis showed a band corresponding to the monomeric form (~56 kDa), while native PAGE indicated a tetrameric oligomer (Figure S5). Gel filtration chromatography (Figure S6A) revealed the oligomeric composition of *Bf*GAD$_{WT}$ at acidic (pH 4.7, blue) and neutral (pH 7.2, red) conditions. At pH 4.7, a major peak (peak 3) corresponded to an intermediate molecular weight (~180 kDa) between a dimer and a tetramer, while, at pH 7.2, the same peak shifted closer to the molecular weight of a dimer (~150 kDa) (Figures S6A–S6C). Peak 2 (~351 kDa) likely represents a hexamer, and peak 1, eluting in the void volume, suggests protein aggregation. The intermediate molecular weights observed may result from the inability to fully resolve the dimeric and tetrameric states. Most microbial GADs studied so far are oligomeric, existing in dimeric, tetrameric, or hexameric states.[39,41–45] Our findings suggest that purified *Bf*GAD$_{WT}$ exhibits behavior consistent with other characterized prokaryotic GADs, with a dynamic equilibrium between dimeric and tetrameric forms. We also observed a pH-dependent shift in the oligomeric forms of *Bf*GAD$_{WT}$, similar to the behavior reported for *E. coli* GAD (*Ec*GAD), which exhibits significant changes in oligomeric composition in response to pH.[45] Furthermore, the addition of external PLP did not alter the oligomeric state of *Bf*GAD$_{WT}$ (Figure S6D).

PLP cofactor bound to the *Bf*GAD$_{WT}$ undergoes pH-dependent tautomeric changes

Spectral studies with *Bf*GAD$_{WT}$ revealed that the enzyme was purified in its holo form with the covalently bound PLP cofactor. There were two absorption maxima observed for *Bf*GAD$_{WT}$—335 and 420 nm (Figure 1B). These absorption maxima likely result from the two tautomeric forms of the enzyme-bound PLP cofactor, enolimine form at 335 nm, and ketoenamine form at 420 nm,[46–48] as shown previously with *E. coli* GAD.[49] The proportions of these tautomers varied with pH (Figure 1B). At lower pH, the 420 nm species dominated, while, at higher pH, the 335 nm species became more prevalent. Increasing the pH from 4.7 to 8.6 resulted in a decrease in the 420 nm species and a concomitant increase in the 335 nm species (Figure 1B). These pH-dependent changes in PLP absorbance closely correlate with enzyme activity, with maximum catalytic efficiency observed at pH 4.7, where the 420 nm absorbing species predominates, and minimal activity occurred at other pH values (Figure S7). Consequently, all subsequent activity assays were performed at pH 4.7. These data are consistent with previously studied microbial GADs highlighting the influence of pH on active site hydration and tautomeric equilibrium.[39,42,49–51] Moreover, analysis of the pH versus absorbance curve at 420 nm suggested that multiple protons influence the transition in absorbance (Figure S7).

Evidence for allosteric regulation of *Bf*GAD$_{WT}$

Activity assays with varying *Bf*GAD$_{WT}$ concentrations demonstrated a linear relationship between initial reaction velocities and enzyme concentrations (Figure 1C). From this plot, the optimal *Bf*GAD$_{WT}$ concentration for subsequent kinetic assays was

determined. Interestingly, while varying L-glutamate concentrations, the plot of substrate concentration versus initial velocity displayed a sigmoidal curve instead of a typical hyperbolic dependence, suggestive of a cooperativity in *Bf*GAD$_{WT}$. Specifically, we hypothesize that the observed sigmoidal curve may arise from a conformational shift that modulates the affinity of the active site for L-glutamate thus providing an example of a homotropic allosteric regulation. From the fit of this plot with the hill equation (Equation 2), the analyzed $K_{0.5}$ (K_{half}) was 8.6 ± 0.4 mM and V_{max} was 0.86 ± 0.04 mM/min with a hill coefficient of 1.7 (Figure 1D). $(K_{half})^h$ is also known as K_{prime} (K′), which is equivalent to K_m from a hyperbolic kinetics of non-allosteric enzymes, when h = 1. However, in cooperative systems where h ≠1 like presented here for *Bf*GAD$_{WT}$, then K′ (K_{half}^h) no longer represents the substrate concentration required to achieve half of maximal velocity. Unlike oligomeric conformations and spectral characteristics, the kinetic parameters of *Bf*GAD$_{WT}$ vary from previously investigated prokaryotic GADs.[39,41–44,52] *Bf*GAD$_{WT}$ displayed a positive cooperativity with the substrate L-glutamate. This aligns with studies on other PLP-dependent and pyruvoyl-dependent decarboxylases, which show that substrate-induced conformational changes can influence their catalytic activity.[53,54] One such example is of a PLP-dependent human ornithine decarboxylase where a catalytically active dimeric functional unit exhibited cooperativity with its substrate.[53] Similarly, a pyruvoyl-dependent histidine decarboxylase displayed sigmoidal kinetics with increasing substrate concentration.[54] While the physiological consequences of this cooperativity in *Bf*GAD need to be explored further, the data suggest that cooperative binding and adaptability might help amplify the response of an enzyme to changes in substrate concentration, possibly making it more sensitive to the physiological substrate concentrations and conditions.

Engineered *Bf*GAD variants exhibit structural and catalytic perturbations

Most microbial GADs are functionally active as dimers, with residues from both monomers contributing to the active site.[39–42] The earliest microbial GAD structures with bound ligands were solved for *E. coli* GADs (GAD*A*: PDB ID 1XEY and GAD*B*: PDB ID 1PMM) (Figure S8).[39,40] Two conserved residues of *Ec*GADs, phenylalanine 63 (F81 in *Bf*GAD$_{WT}$) and aspartate 86 of the neighboring subunit (D104 in *Bf*GAD$_{WT}$), make hydrogen bonds with one of the carboxylates of ligands. Specifically, in GAD*B*, carboxylate of acetate forms H-bonds with the amide nitrogen of F63 (F81 in *Bf*GAD$_{WT}$) and the carboxylate side chain of D86 (D104 in *Bf*GAD$_{WT}$), while, in GAD*A*, carboxylate of glutarate interacts similarly with these residues.[39,40] These residues are conserved across most gut microbial GADs, except for *Eggerthella lenta*, which lacks a conserved phenylalanine (Figure S3). Key residues for rational evolution of *Bf*GAD$_{WT}$ were then selected based on interactions of ligands with *Ec*GADs[39,40,55] (Figure S8B) and a recently solved ligand-bound structure of glutamate decarboxylase (*Bt*GAD) from *Bacteroides thetaiotaomicron*.[42] Specifically, structural alignments of glutarate-bound *Ec*GAD*A* (PDB ID 1XEY) and *Bt*GAD (PDB ID 7X51) with the *Bf*GAD$_{WT}$ dimer (created using AlphaFold2) guided the engineering of two *Bf*GAD$_{WT}$ variants: D104N and F81W, designed to test substrate preference. Figures 2A and 2B highlight the active site positions of F81 and D104 in *Bf*GAD$_{WT}$ (green), superimposed with PLP and glutarate from *Ec*GAD*A*. Similarly, Figures 2C and 2D show aligned structures of *Bf*GAD$_{WT}$ and *Bt*GAD with PLP and glutarate bound. The structures of variants *Bf*GAD$_{D104N}$ and *Bf*GAD$_{F81W}$ were also superimposed with ligand-bound *Ec*GAD and *Bt*GAD structures, as shown in Figure 2.

The AlphaFold model predicts active site architecture of *Bf*GAD that is largely similar to *Ec*GAD and *Bt*GAD, though positional shifts were observed, particularly for aspartate (D104), which differed significantly between *Ec*GAD and *Bf*GAD. However, substitutions introduced in the engineered variants *Bf*GAD$_{D104N}$ and *Bf*GAD$_{F81W}$ altered H-bonding interactions between the substrate analog and active site residues. Despite structural differences observed in the overlay, both variants were successfully purified as holoenzymes (PLP-bound form) under the same conditions as *Bf*GAD$_{WT}$ and retained activity. Ultraviolet-visible (UV-vis) spectra at pH 4.7 revealed absorption maxima at 335 and 420 nm for all three enzymes, with variations in the relative proportions of these species (Figure 2E). In addition, progress curve analysis for the decarboxylation of L-glutamate showed differing initial velocities where *Bf*GAD$_{D104N}$ exhibited a 1.7-fold increase, while *Bf*GAD$_{F81W}$ showed a 2.5-fold decrease compared to *Bf*GAD$_{WT}$ (Figure 2F). These observed differences in catalysis by *Bf*GAD variants highlight the importance of F81 and D104 in substrate interaction and demonstrate the impact of structural perturbations caused by these substitutions. With these observations, we hypothesized that the changes in these H-bonding interactions could potentially provide a way to evolve new activity or specificity in engineered *Bf*GADs.

Wild-type and engineered *Bf*GADs can decarboxylate substrates other than L-glutamate

Our initial assays showed that the purified *Bf*GAD$_{WT}$ is able to catalyze the conversion of L-glutamate to GABA. As a first step to test our aforementioned outlined hypothesis, we conducted activity assays with D-glutamate. We find that both the wild-type and engineered *Bf*GADs were unable to decarboxylate D-glutamate (Figure S9). Microbial GADs from various genera[39,41,43,56,57] show high substrate specificity toward L-glutamate,[41,52,58,59] but instances of substrate promiscuity are also found. For example, *E. coli* GAD can convert a phosphinic analog of glutamate to a phosphinic analog of GABA[60]; archaeal GADs can decarboxylate L-aspartate and L-cysteate[61,62]; and certain mammalian GADs and their homologs can decarboxylate one or more of the non-native substrates such as L-aspartate, L-cysteate, and L-cysteine sulfinate to produce β-alanine, taurine, and hypotaurine from their respective substrates.[63–67] Interestingly, mammals have additional *de novo* pathways for the production of taurine and hypotaurine, which primarily involves the enzyme cysteine sulfinic acid decarboxylase (CSAD) that generates taurine and its intermediate hypotaurine by decarboxylating either L-cysteic acid (CA) or L-cysteine sulfinic acid (CSA).[65,68] In addition, mammalian GADL1 (glutamic acid decarboxylase like 1) with very high sequence similarity to CSAD, is also capable of producing taurine.[63,69] Alongside, mammalian GADL1 is also able to generate β-alanine from L-aspartate.[63,69] β-alanine is a

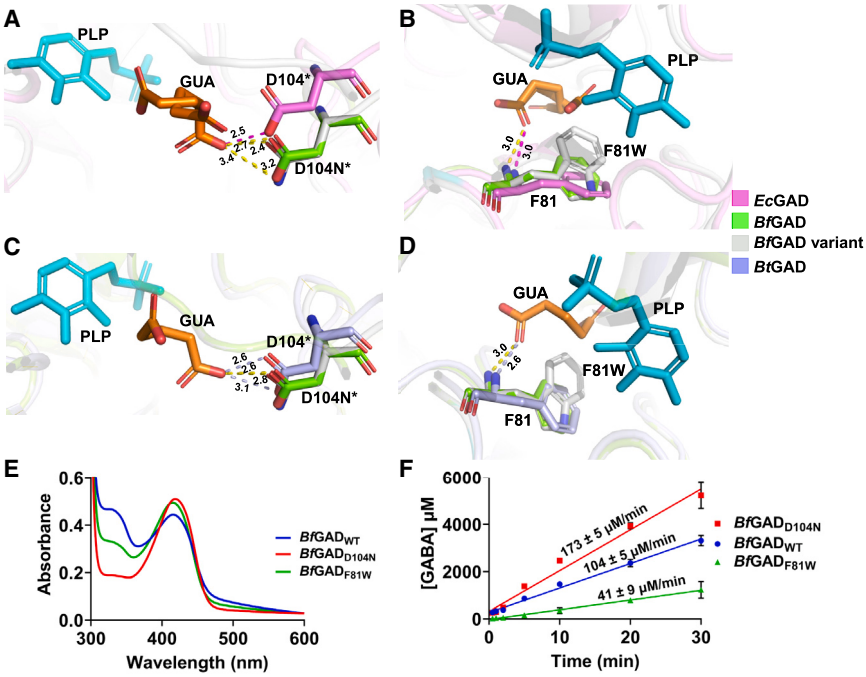

Figure 2. Structural and catalytic perturbations of engineered *Bf*GADs

(A) Aligned structures of *Ec*GAD (1XEY, pink), *Bf*GAD$_{WT}$ (model, green) illustrating the position of the residue D104* (*residue from the neighboring monomer), and *Bf*GAD$_{D104N}$ depicting the point substitution D104N*(model, gray).

(B) Aligned structures of *Ec*GAD (1XEY, pink), *Bf*GAD$_{WT}$ (model, green) illustrating the position of the residue F81, and *Bf*GAD$_{F81W}$ depicting the point substitution F81W (model, gray).

(C) Aligned structures of *Bt*GAD (7X51, purple), *Bf*GAD$_{WT}$ (model, green) illustrating the position of the residue D104* (*residue from the neighboring monomer), and *Bf*GAD$_{D104N}$ depicting the point substitution D104N*(model, gray).

(D) Aligned structures of *Bt*GAD (7X51, purple), *Bf*GAD$_{WT}$ (model, green) illustrating the position of the residue F81, and *Bf*GAD$_{F81W}$ depicting the point substitution F81W (model, gray). The dashed lines indicate hydrogen bond interactions of the amino acid residues with substrate analog, glutarate (GUA), where pink bonds are for interactions between *Ec*GAD-GUA, yellow bonds are for interactions between *Bf*GAD-GUA, and purple bonds are for interactions between *Bt*GAD-GUA.

(E) Spectra of PLP cofactor bound to the holoenzymes *Bf*GAD$_{WT}$ and engineered variants, depicting tautomers of internal aldimine at 335 and 420 nm.

(F) Progress curves depicting initial velocities for reactions catalyzed by *Bf*GAD$_{WT}$ and variants (n = 3). Error bars represent SD.

precursor for the dipeptide beta-alanyl-L-histidine in humans, commonly known as carnosine. Carnosine is found in muscles and brain tissues at high concentrations.[70,71] In microbes, β-alanine is a precursor for coenzyme A biosynthesis, which is an important molecule in various metabolic pathways.[72] Both carnosine and β-alanine show protective effects in individuals with cognitive deficits and Alzheimer's.[73–75] Moreover, higher serum concentrations of β-alanine prevent dementia.[73] Considering the structural similarities between L-glutamate and L-aspartate and the ability of some GADs to use L-aspartate as a substrate,[61,64,76] we hypothesized that *Bf*GAD might be able to produce β-alanine via the decarboxylation of L-aspartate (Scheme 1).

In contrast to GAD, most prokaryotes (except for some marine microbes) lack the major *de novo* pathway for taurine formation via CSAD.[67] Interestingly, in these microbes, CSAD genes are present in the operon containing cysteine dioxygenase (CDO) enzyme that catalyzes the conversion of L-cysteine to L-CSA, which then can be converted to hypotaurine and taurine (Figure S15). CDOs are not present in the members of the human gut microbiome possibly due to the hypoxic and anaerobic conditions of the gut. Despite an extensive bioinformatics search, we did not find any gut microbial genes annotated as CSAD. Due to the lack of the annotated CSAD enzymes responsible for the *de novo* taurine biosynthesis, we further hypothesized that *Bf*GAD might be involved in the formation of taurine and its derivatives in addition to GABA by using L-CA (cysteate), L-CSA (cysteine sulfinate), and L-HCA (homocysteate) (Scheme 1).

If *Bf*GAD$_{WT}$ or engineered *Bf*GADs are able to decarboxylate substrates other than the native substrate L-glutamate, then the detection of the common product CO_2 will be a positive indicator for the utilization of other substrates (Scheme 1). For this reason, we used a headspace gas chromatography (GC) to detect the CO_2 evolved from reactions catalyzed by either *Bf*GAD$_{WT}$ or engineered *Bf*GADs with five different substrates (Figure 3). CO_2 peaks produced by the reactions of *Bf*GAD$_{WT}$, *Bf*GAD$_{D104N}$, and *Bf*GAD$_{F81W}$ with five different substrates were visible with gas chromatograms immediately after 12.8 min (Figures 3A, 3C, and 3E). Interestingly, CO_2 peak areas from the decarboxylation reactions of the substrates after 24 h incubation with *Bf*GAD$_{WT}$ showed significant production of CO_2 generated from the decarboxylation of both L-glutamate (blue) and L-CSA (red) (Figures 3A and 3B). To our knowledge, this is the first indication of a gut microbial GAD that can utilize L-CSA as a substrate.

We also found that *Bf*GAD$_{WT}$ was capable of decarboxylating L-HCA (orange) and L-CA (green), albeit to a smaller extent, and was able to decarboxylate L-aspartate (purple) (Figures 3A and 3B). Relative to the CO_2 production peak area with the native substrate L-glutamate for *Bf*GAD$_{WT}$, we observed 54%, 3%, 6%, and 20% of CO_2 production with L-CSA, L-CA, L-HCA, and L-Asp, respectively, within 24 h, which increased to 75% (L-CSA), 6% (L-CA), 7% (L-HCA), and 28% (L-Asp), respectively, within 48 h (Figure S10A).

For *Bf*GAD$_{D104N}$, CO_2 production is comparable to the *Bf*GAD$_{WT}$ while using native substrate L-glutamate. Compared to the peak area of CO_2 production for L-glutamate (native substrate), we observed around 16%, 11%, 3%, and 7% CO_2 production from L-CSA, L-CA, L-HCA, and L-aspartate, respectively, within 24 h (Figures 3C and 3D) that increased to 18% for both L-CSA and L-CA and 7% for L-HCA and slightly decreased

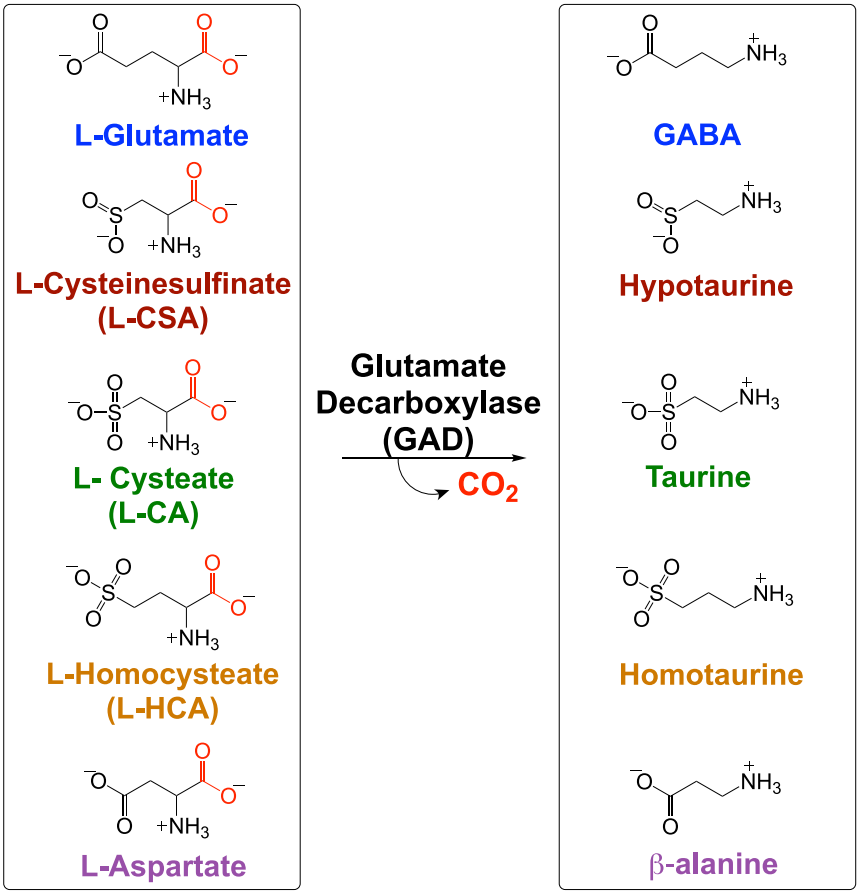

Scheme 1. Predicted substrates and products of *Bf*GAD-catalyzed decarboxylations

with L-aspartate within 48 h (Figure S10B). Based on the data collected with *Bf*GAD$_{WT}$ and *Bf*GAD$_{D104N}$, we find that the residue Asp104 (D104) from the neighboring monomer plays a crucial role in accommodating various substrates. This engineered enzyme was also able to decarboxylate L-CSA, L-HCA, and L-Asp in addition to the native substrate L-glutamate but less efficiently than *Bf*GAD$_{WT}$, and, specifically, the activity toward L-CSA was significantly impacted. It is likely that the negative charge of the side-chain carboxylate from D104 is important for the specificity toward alternative substrates L-CSA, L-HCA, and L-Asp but not for the native substrate L-glutamate. As a result, when the charge was removed due to the substitution of Asp (D) to Asn (N) at position 104, the catalysis with these alternate substrates was affected, but not with the native substrate L-glutamate. Interestingly, we noticed a 2- to 2.5-fold increase in the production of taurine with this evolved enzyme compared to *Bf*GAD$_{WT}$ (Figure 3D), indicating that the substitution from D to N was favorable for taurine production.

The second engineered enzyme, *Bf*GAD$_{F81W}$ retained its activity with the native substrate L-glutamate, but, as demonstrated by its initial velocity measurement, it was slower compared to *Bf*GAD$_{WT}$ (Figure 2F). Relative to the CO_2 peak area of *Bf*GAD$_{WT}$ or *Bf*GAD$_{D104N}$ with the native substrate L-glutamate, *Bf*GAD$_{F81W}$ showed the peak area of around 93%. Additionally, there was minimal decarboxylation activity of *Bf*GAD$_{F81W}$ with L-CA, L-HCA, and L-Asp. However, this evolved enzyme still retained considerable decarboxylation activity with L-CSA (Figures 3E and 3F). It is interesting to note that a bulky substitution of tryptophan (W) at position 81, instead of phenylalanine (F), made the enzyme more specific toward the native substrate L-glutamate (Figures 2B and 2D). Our GC data suggest that the substrate preference for *Bf*GAD$_{WT}$ was L-Glu > L-CSA > L-Asp > L-HCA > L-CA that changed to L-Glu > L-CSA ≥ L-CA > L-Asp > L-HCA for *Bf*GAD$_{D104N}$. However, for *Bf*GAD$_{F81W}$, only L-glutamate and L-CSA showed decarboxylation while L-glutamate was a much better substrate than L-CSA. Absolute quantification of $CO_{2(g)}$ was challenging due to its high solubility at acidic pH where we conducted our enzymatic reactions. In these conditions, the CO_2 produced through the reaction might still be in a soluble form as a dissolved CO_2. So, headspace GC was utilized as a tool to identify alternate substrates by allowing detection of CO_2 peak that served as a preliminary confirmation of our hypothesis by providing indication of enzymatic decarboxylation of diverse substrates by the wild-type and variants of *Bf*GAD.

Wild-type and evolved *Bf*GADs produce multiple neuromodulatory molecules

The generation of CO_2 in reactions facilitated by *Bf*GAD$_{WT}$ and its engineered variants prompted further testing of our hypothesis via the detection and identification of products resulting from decarboxylation with diverse substrates. Both *Bf*GAD$_{WT}$ and *Bf*GAD$_{D104N}$ appear to produce decarboxylated products—hypotaurine, taurine, homotaurine, and β-alanine from substrates L-CSA, L-CA, L-HCA, and L-Asp, respectively (Figures 4A–4D; Figures S11A–S11D). Chromatograms showed that *Bf*GAD$_{WT}$ decarboxylated L-CSA and L-Asp to produce hypotaurine and β-alanine more efficiently than *Bf*GAD$_{D104N}$ (Figures 4A and 4C). However, *Bf*GAD$_{D104N}$ was better at decarboxylating L-CA to taurine than *Bf*GAD$_{WT}$ (Figure 4B). We do not observe much of decarboxylated product taurine with *Bf*GAD$_{WT}$ from L-CA decarboxylation during 24 h incubation, whereas *Bf*GAD$_{D104N}$ shows a significant production of taurine during this time frame (Figures 4B and S11E). While our CO_2 evolution experiments have shown that *Bf*GAD$_{WT}$ can catalyze L-CA decarboxylation in 24 h, the failure to observe decarboxylated product may be attributed to the low concentration of taurine produced, making it undetectable on a thin-layer chromatography (TLC) plate. Both enzymes

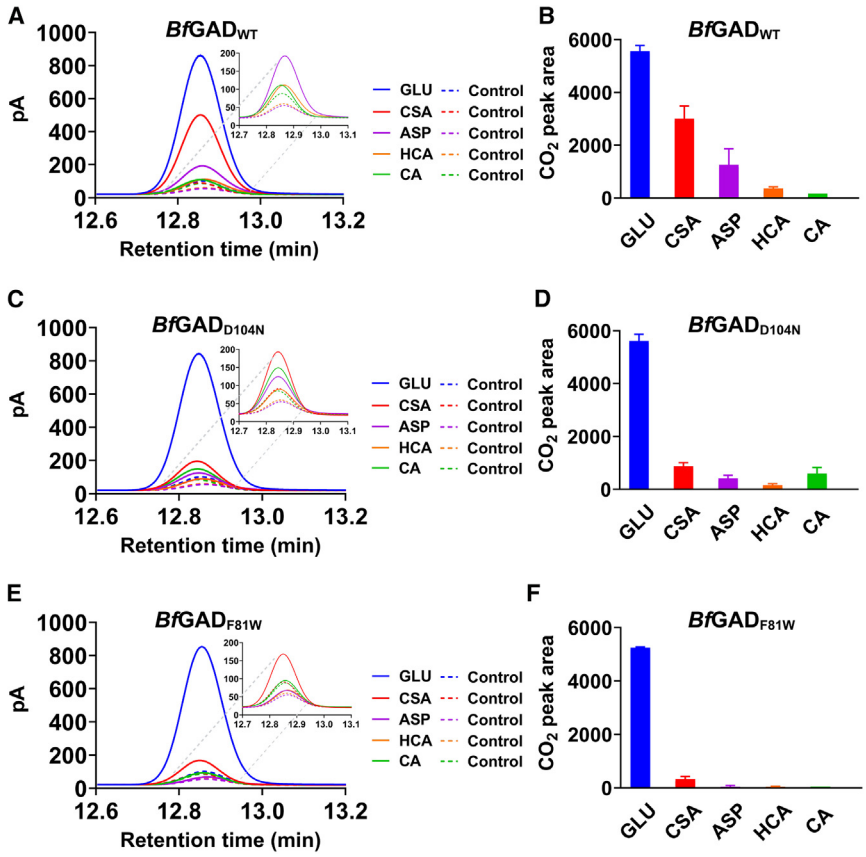

Figure 3. Wild-type and engineered *Bf*GADs can decarboxylate multiple substrates

(A, C, and E) Chromatograms showing the CO_2 peaks obtained from the decarboxylation reactions of multiple substrates after 24 h incubation with (A) *Bf*GAD$_{WT}$, (C) *Bf*GAD$_{D104N}$, and (E) *Bf*GAD$_{F81W}$ using headspace GC (n = 3, only one representative CO_2 peak is depicted for every reaction).

(B, D, and F) The CO_2 peak areas are depicted for the decarboxylation of various substrates after 24 h incubation with (B) *Bf*GAD$_{WT}$, (D) *Bf*GAD$_{D104N}$, and (F) *Bf*GAD$_{F81W}$. Error bars represent SD (n = 3).

Various substrates are presented as specific colors, which are consistent in all panels where L-glutamate is blue, L-CSA is red, L-Asp is purple, L-HCA is orange, and L-CA is green.

*Bf*GAD$_{WT}$ and *Bf*GAD$_{D104N}$ were able to catalyze the decarboxylation of L-HCA to homotaurine to a very small extent (Figure 4D). We also verified that the product from the L-Asp decarboxylation was β-alanine and not L-alanine. Although, the R_f (retention factor) values were almost similar for β-alanine and L-alanine, the staining with ninhydrin differs for these molecules. β-alanine exhibited a purple color whereas L-alanine shows a brick red color with ninhydrin stain (Figure S11C). Despite the detection of CO_2 during the decarboxylation activity of *Bf*GAD$_{F81W}$ with L-CSA (Figure 3F), we did not observe detectable hypotaurine spots on the TLC plate (Figure S12A). It is possible that the low hypotaurine produced by *Bf*GAD$_{F81W}$ may not be within the mM range required for our assay. As expected, we did not find any activity of *Bf*GAD$_{F81W}$ with L-CA, L-Asp, and L-HCA, and, in line with GC data, we did not detect taurine, β-alanine, and homotaurine even after 48 h incubation (Figure S12A and S12B). The data presented here, along with the GC data (Figure 3), support the conclusion that *Bf*GAD is capable of producing a range of compounds with known neuromodulatory activity.

*Bf*GAD$_{WT}$ and *Bf*GAD$_{D104N}$ generate neuromodulatory molecules at differential abundances, even when presented with a mixed substrate pool

In a complex gut environment, a microorganism encounters multiple substrates simultaneously. To investigate how *Bf*GAD$_{WT}$ functions in a complex environment, we conducted competition assays between various substrates. The presence of decarboxylated products in mixtures containing the native substrate L-glutamate with a specific alternate substrate was detected. The data with *Bf*GAD$_{WT}$ indicate that when the concentration ratio of the native substrate to the alternative substrate was 1:1, GABA was predominantly seen as the primary decarboxylated product (Figure S13F). However, when the concentration ratios were changed to 1:5 (L-Glu with L-CSA/L-Asp) and 1:10 (L-Glu with L-CSA/L-CA/L-Asp), a gradual increase over time was observed in the formation of the alternative decarboxylated products—hypotaurine, taurine, and β-alanine (Figures 5, 6, and 7). For the *Bf*GAD$_{WT}$-catalyzed decarboxylation reactions of L-CSA and L-Asp, the resulting products hypotaurine and β-alanine could be observed when these substrates were in 5-fold excess to the native substrate L-glutamate. However, the accumulation of products hypotaurine and β-alanine becomes significant only after 9 h (for β-alanine) to 24 h (for hypotaurine) (Figures S13D and S13E). In contrast, when L-CSA and L-Asp are used in 10-fold excess of L-glutamate, the resulting products, hypotaurine and β-alanine (peaks highlighted in pink), started accumulating significantly much earlier around 3 h (Figures 5 and 7). We did not observe the accumulation of taurine even when 10-fold excess of L-CA was mixed with L-glutamate in the *Bf*GAD$_{WT}$-catalyzed reaction (Figure 6). However, as mentioned earlier, we were able to detect CO_2 in the same time frame (48 h) in the reaction catalyzed by *Bf*GAD$_{WT}$ when L-CA was provided as the sole substrate (Figure S10A). The inability to detect taurine might be because of the low concentrations produced under the competitive environment of the mixed substrate pool. Unlike *Bf*GAD$_{WT}$, *Bf*GAD$_{D104N}$ was able to decarboxylate and accumulate taurine (peaks highlighted in pink) to a small extent when L-CA is mixed with L-glutamate at a 10-fold excess concentration, especially between 24 and 48 h (Figure 6). Interestingly, in all mixed substrate experiments, we observed

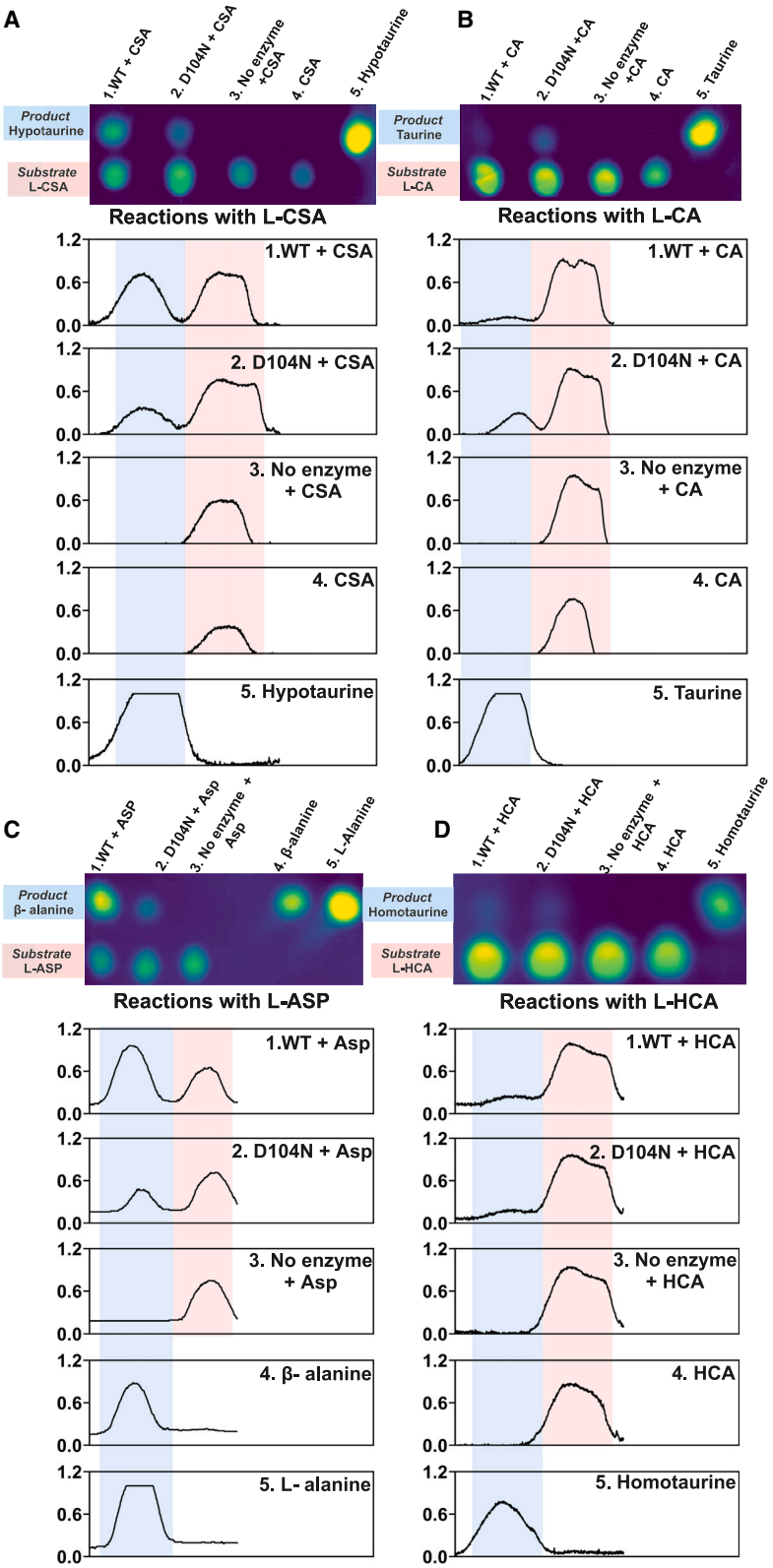

Figure 4. Production of multiple neuromodulatory molecules by wild-type and evolved *Bf*GADs

Intensity analysis of TLC plates depicting intensity plots for each lane. The peak size is proportional to the intensity of the sample spot on the TLC plate.

(A) Production of hypotaurine from the decarboxylation of L-CSA catalyzed by *Bf*GAD$_{WT}$ and *Bf*GAD$_{D104N}$ in 24 h as indicated by TLC intensity analysis. For intensity plots, peaks highlighted in pink are for the substrate L-CSA and peaks highlighted in blue are for the product hypotaurine.

(B) Production of taurine from the decarboxylation of L-CA catalyzed by *Bf*GAD$_{WT}$ and *Bf*GAD$_{D104N}$ in 24 h as indicated by TLC intensity analysis. For intensity plots, peaks highlighted in pink are for the substrate L-CA and peaks highlighted in blue are for the product taurine.

(C) Production of β-alanine from the decarboxylation of L-Asp catalyzed by *Bf*GAD$_{WT}$ and *Bf*GAD$_{D104N}$ in 24 h as indicated by TLC intensity analysis. For intensity plots, peaks highlighted in pink are for the substrate L-Asp and peaks highlighted in blue are for the product β-alanine.

(D) Production of homotaurine from the decarboxylation of L-HCA catalyzed by *Bf*GAD$_{WT}$ and *Bf*GAD$_{D104N}$ in 24 h as indicated by TLC intensity analysis. For intensity plots, peaks highlighted in pink are for the substrate L-HCA and peaks highlighted in blue are for the product homotaurine.

The original TLC plates are shown in Figure S11.

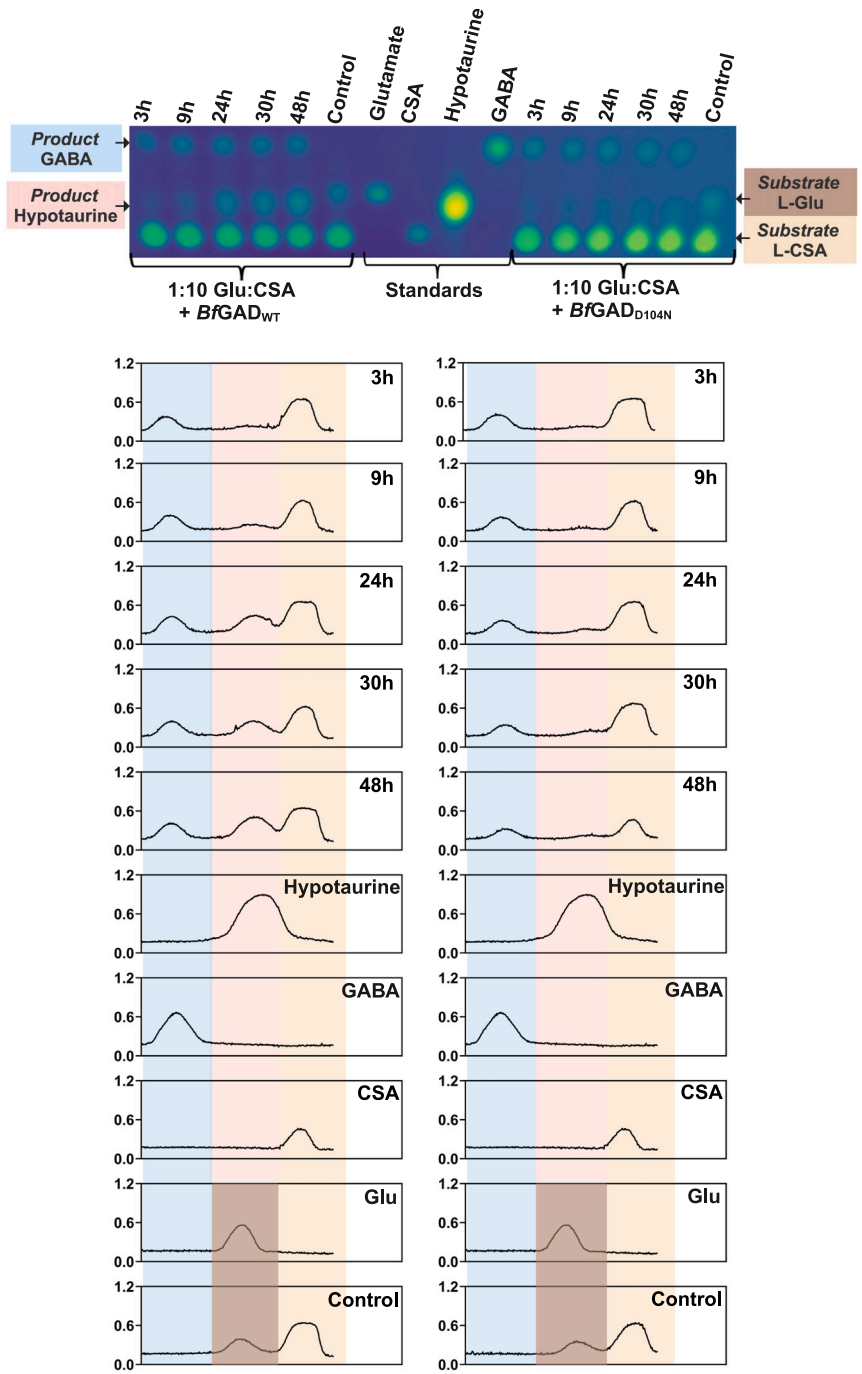

Figure 5. *Bf*GAD$_{WT}$ and *Bf*GAD$_{D104N}$ generate hypotaurine when presented with a mixture of L-glutamate and L-CSA

Intensity analysis of TLC plates for various time points of decarboxylation reactions catalyzed by *Bf*GAD$_{WT}$ and *Bf*GAD$_{D104N}$ for mixed substrates where the concentration ratio of L-glutamate to L-CSA is 1:10. Standards of L-glutamate, L-CSA, GABA, and hypotaurine were included as references. Production of hypotaurine (peaks highlighted in pink) can be seen as the peak area increases over time. GABA peaks are highlighted in blue, peaks for the substrate L-CSA are highlighted in beige, and peaks for the substrate L-glutamate are in brown. Spots visible on TLC plates from top to bottom show corresponding intensity peaks from left to right.

maximum accumulation of the native product GABA (peaks highlighted in blue) within 3 h. The intensity peaks showed no further increase after 3 h time point. This shows that even in the presence of other substrates the native activity of L-glutamate decarboxylation occurred at the highest velocity for all *Bf*GADs compared to the decarboxylation reactions of other substrates.

The decarboxylated products hypotaurine and taurine were analyzed using liquid chromatography-electrospray ionization-tandem mass spectrometry (LC-ESI-MS/MS) to confirm their presence and mass in mixed substrate assays where L-glutamate to L-CSA or L-CA ratios were 1:10, which confirmed the results of the TLC data. The qualitative analysis of these molecules was conducted using multiple reaction monitoring (MRM) mode by running mixed standards (Figure S14). The native substrate and product, L-glutamate and GABA, in these samples were previously confirmed by both TLC and GABase assay prior to liquid chromatography-tandem mass spectrometry (LC-MS/MS) analysis. The product hypotaurine and the remaining L-CSA substrate were present in the mixed substrate reactions with a 1:10 ratio of L-glutamate:L-CSA catalyzed by *Bf*GAD$_{WT}$ (Figure 8A) whereas taurine and remaining L-CA were found in the mixed substrate reactions with a 1:10 ratio of L-glutamate:L-CA catalyzed by *Bf*GAD$_{D104N}$ (Figure 8B).

In conclusion, we report that *Bf*GAD$_{WT}$ is a promiscuous enzyme capable of decarboxylating four additional substrates, structurally similar to L-glutamate, to produce known neuromodulatory molecules such as hypotaurine, taurine, homotaurine, and β-alanine. Through rational enzyme engineering, we generated an evolved *Bf*GAD variant that produces twice as much taurine as the wild-type enzyme. These findings open up new avenues for developing novel biocatalysts and exploring therapeutic applications, as well as for scaling up the enzymatic production of neuromodulatory compounds by microbes that reside in the gut. Future work will focus on investigating the physiological significance of these *Bf*GAD-derived neuromodulatory compounds in animal models, as well as optimizing the specificity and catalytic efficiency of *Bf*GAD for potential therapeutic applications.

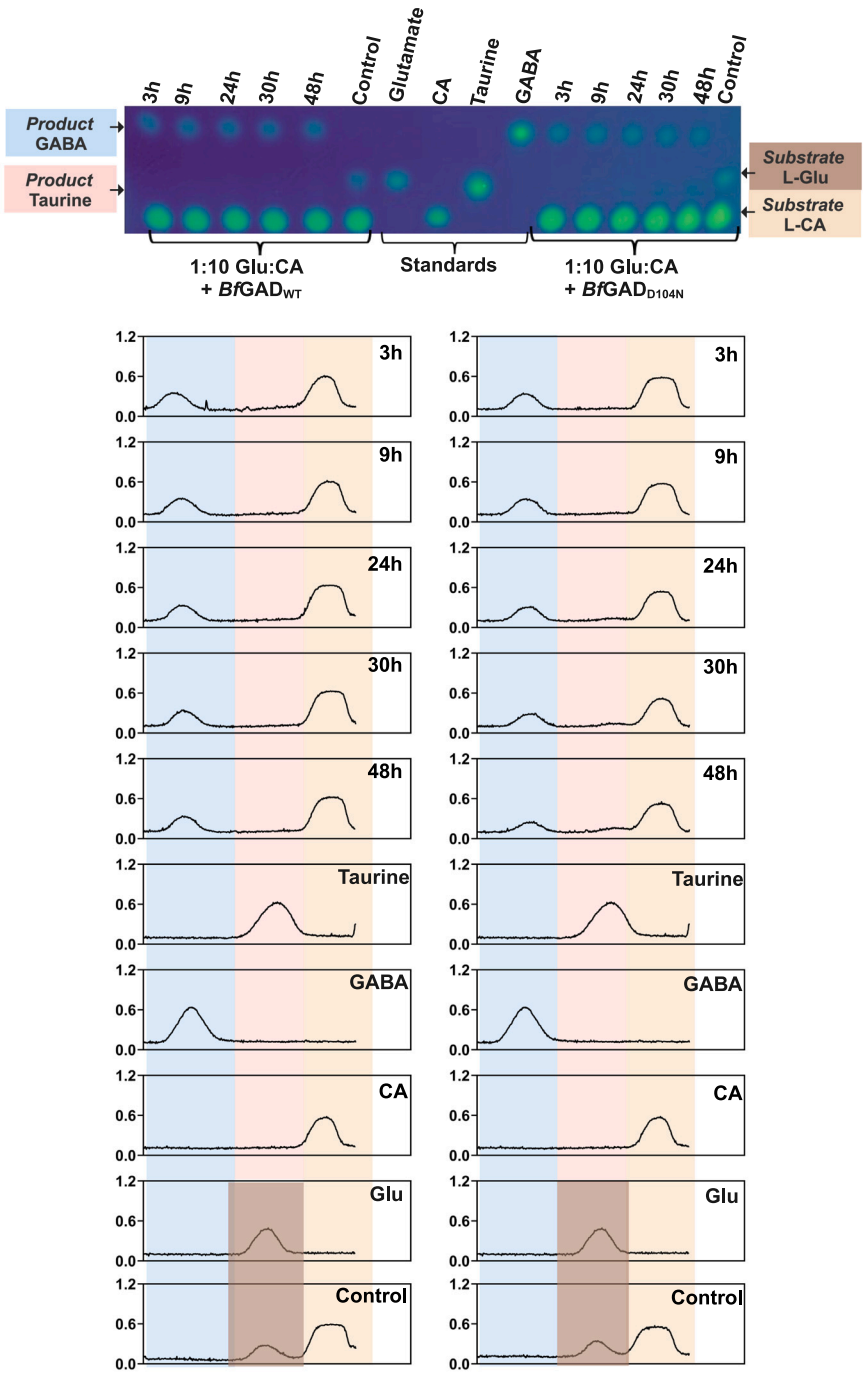

Figure 6. *Bf*GAD$_{D104N}$ generates taurine when presented with a mixture of L-glutamate and L-CA

Intensity analysis of TLC plates for various time points of decarboxylation reactions catalyzed by *Bf*GAD$_{WT}$ and *Bf*GAD$_{D104N}$ for mixed substrates where the concentration ratio of L-glutamate to L-CA is 1:10. Standards of L-glutamate, L-CA, GABA, and taurine were included as references. Production of taurine (peaks highlighted in pink) can be seen as the peak area increases over time for *Bf*GAD$_{D104N}$-catalyzed reactions. GABA peaks are highlighted in blue, peaks for the substrate L-CA are highlighted in beige, and peaks for the substrate L-glutamate are in brown. Spots visible on TLC plates from top to bottom show corresponding intensity peaks from left to right.

Limitations of the study

Current limitations include the reliance on AlphaFold2-predicted *Bf*GAD structures, which might limit the accuracy of conformations for the wild-type and engineered *Bf*GADs. In addition, reaction kinetics for substrates other than L-glutamate remain unknown with all studied *Bf*GADs. A deeper understanding of the capacity of *B. fragilis* to produce and secrete these neuromodulatory molecules is necessary before pursuing potential biotherapeutic applications.

RESOURCE AVAILABILITY

Lead contact

Further information and requests for resources should be directed to the lead contact, Dhara D. Shah (dhara.shah1@asu.edu).

Materials availability

There are restrictions to the availability of plasmids to generate *Bf*GAD variant enzymes or purified preparations of these variant forms due to a pending patent application.

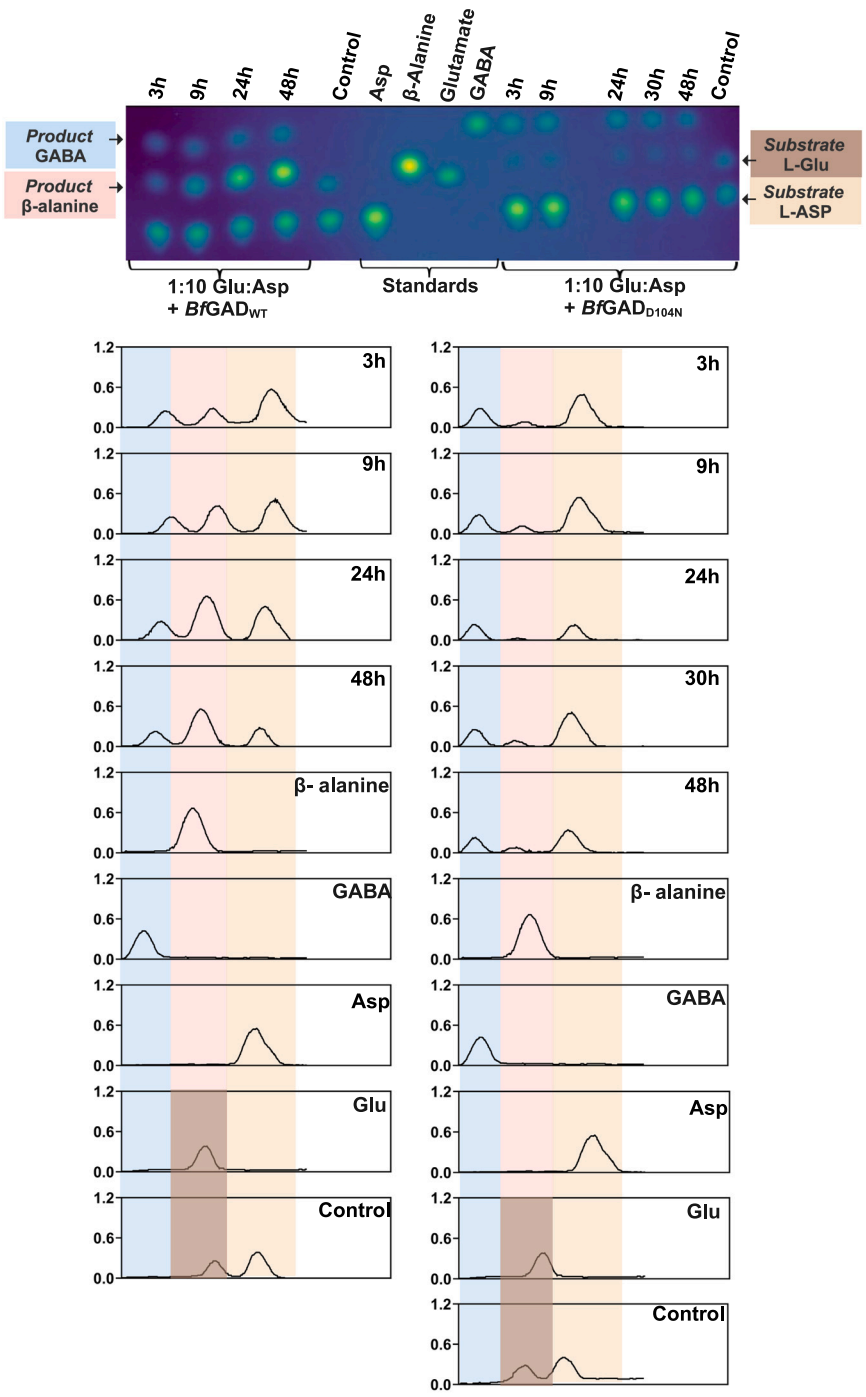

Figure 7. *Bf*GAD$_{WT}$ and *Bf*GAD$_{D104N}$ generate β-alanine when presented with a mixture of L-glutamate and L-aspartate

Intensity analysis of TLC plates for various time points of decarboxylation reactions catalyzed by *Bf*GAD$_{WT}$ and *Bf*GAD$_{D104N}$ for mixed substrates where the concentration ratio of L-glutamate to L-aspartate is 1:10. Standards of L-glutamate, L-aspartate, GABA, and β-alanine were included as references. Production of β-alanine (peaks highlighted in pink) can be seen as the peak area increases over time. The increase over time for *Bf*GAD$_{D104N}$ is very clear from 3 to 9 h. Due to the differences in the background intensity of the TLC plate in areas containing 3 and 9 h samples vs. areas containing 24, 30, and 48 h samples from *Bf*GAD$_{D104N}$-catalyzed reaction, the increase in the intensity peak is not uniform. GABA peaks are highlighted in blue, peaks for the substrate L-aspartate (L-Asp) are highlighted in beige, and peaks for the substrate L-glutamate are in brown. Spots visible on TLC plates from top to bottom show corresponding intensity peaks from left to right.

Data and code availability

- All the data reported in this article will be shared by the lead contact upon request.
- The original code generated in this study has been deposited at Zenodo and GitHub and is publicly available as of the date of publication. The URL is listed in the key resources table.
- Any additional information required to reanalyze the data reported in this paper is available from the lead contact upon request.

ACKNOWLEDGMENTS

This research is supported by the seed grant from Edson Initiative for Dementia Care and Solutions to D.D.S. A.S. was supported by an NIH-NIGMS MIRA award R35GM147131. We acknowledge resources and support from the Knowledge Enterprise Biosciences Core Facilities at Arizona State University. We also thank Dr. Rosa Krajmalnik-Brown and Christopher Muse from the Biodesign Center for Health Through Microbiomes for the help with headspace GC. All figures were created using BioRender.com.

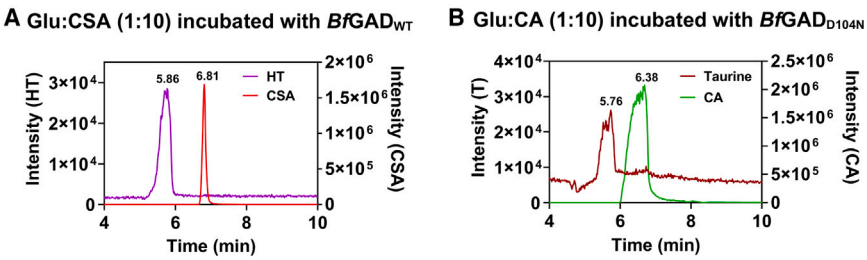

Figure 8. Hypotaurine and taurine detection via LC-MS/MS from *Bf*GAD$_{WT}$- and *Bf*GAD$_{D104N}$-catalyzed mixed substrate reactions

(A) Ion chromatograms of product hypotaurine and the remaining L-CSA substrate in the mixed substrate reactions with a 1:10 ratio of L-glutamate:L-CSA catalyzed by *Bf*GAD$_{WT}$.

(B) Ion chromatograms of taurine and remaining L-CA in the mixed substrate reactions with a 1:10 ratio of L-Glutamate:L-CA catalyzed by *Bf*GAD$_{D104N}$.

AUTHOR CONTRIBUTIONS

P.D. and D.D.S. conceptualized the project. D.D.S. secured funding and supervised the research. P.D. performed majority of the experiments and data analysis. C.W.P. performed some of the TLC experiments. A.S. performed analysis and data fitting for pH and Abs variation experiment and provided code and advice on the image analysis of TLC plates. P.D. and D.D.S. wrote the manuscript with contributions and discussions from all other authors.

DECLARATION OF INTERESTS

Aspects of this research are part of a pending patent application.

STAR★METHODS

Detailed methods are provided in the online version of this paper and include the following:

- KEY RESOURCES TABLE
- EXPERIMENTAL MODEL AND STUDY PARTICIPANT DETAILS
- METHOD DETAILS
  - Gene cloning
  - Expression and purification of *Bf*GAD$_{WT}$ and engineered *Bf*GADs
  - Gel filtration chromatography with *Bf*GAD$_{WT}$
  - Activity assays
  - *Bf*GAD absorbance spectrophotometry and activity assays with pH variation
  - Steady-state kinetics
  - Generation of engineered *Bf*GAD variants
  - $CO_{2(g)}$ detection by headspace gas chromatography
  - Thin layer chromatography (TLC)
  - Liquid chromatography with tandem mass spectrometry (LC-MS/MS) detection of decarboxylated products from reactions catalyzed by *Bf*GADs (WT and engineered variants)
  - Multiple sequence alignment and phylogenetic analyses of gut microbial GADs
  - *Bf*GAD dimer generation with the AlphaFold2 and visualization, structural alignments, and mutagenesis via PyMOL
- QUANTIFICATION AND STATISTICAL ANALYSIS

SUPPLEMENTAL INFORMATION

Supplemental information can be found online at https://doi.org/10.1016/j.isci.2025.112289.

Received: October 23, 2024
Revised: January 14, 2025
Accepted: March 21, 2025
Published: March 25, 2025

REFERENCES

1. Murley, A.G., Rouse, M.A., Jones, P.S., Ye, R., Hezemans, F.H., O'Callaghan, C., Frangou, P., Kourtzi, Z., Rua, C., Carpenter, T.A., et al. (2020). GABA and glutamate deficits from frontotemporal lobar degeneration are associated with disinhibition. Brain *143*, 3449–3462. https://doi.org/10.1093/brain/awaa305.

2. Nuss, P. (2015). Anxiety disorders and GABA neurotransmission: a disturbance of modulation. Neuropsychiatr. Dis. Treat. *11*, 165–175. https://doi.org/10.2147/NDT.S58841.

3. Cawley, N., Solanky, B.S., Muhlert, N., Tur, C., Edden, R.A.E., Wheeler-Kingshott, C.A.M., Miller, D.H., Thompson, A.J., and Ciccarelli, O. (2015). Reduced gamma-aminobutyric acid concentration is associated with physical disability in progressive multiple sclerosis. Brain *138*, 2584–2595. https://doi.org/10.1093/brain/awv209.

4. Goddard, A.W., Mason, G.F., Almai, A., Rothman, D.L., Behar, K.L., Petroff, O.A., Charney, D.S., and Krystal, J.H. (2001). Reductions in occipital cortex GABA levels in panic disorder detected with 1h-magnetic resonance spectroscopy. Arch. Gen. Psychiatry *58*, 556–561. https://doi.org/10.1001/archpsyc.58.6.556.

5. Goddard, A.W., Mason, G.F., Appel, M., Rothman, D.L., Gueorguieva, R., Behar, K.L., and Krystal, J.H. (2004). Impaired GABA neuronal response to acute benzodiazepine administration in panic disorder. Am. J. Psychiatry *161*, 2186–2193. https://doi.org/10.1176/appi.ajp.161.12.2186.

6. Long, Z., Medlock, C., Dzemidzic, M., Shin, Y.W., Goddard, A.W., and Dydak, U. (2013). Decreased GABA levels in anterior cingulate cortex/medial prefrontal cortex in panic disorder. Prog. Neuropsychopharmacol. Biol. Psychiatry *44*, 131–135. https://doi.org/10.1016/j.pnpbp.2013.01.020.

7. Orhan, F., Fatouros-Bergman, H., Goiny, M., Malmqvist, A., Piehl, F., Karolinska Schizophrenia Project KaSP Consortium, Cervenka, S., Collste, K., Victorsson, P., Sellgren, C.M., et al. (2018). CSF GABA is reduced in first-episode psychosis and associates to symptom severity. Mol. Psychiatry *23*, 1244–1250. https://doi.org/10.1038/mp.2017.25.

8. Sarlo, G.L., and Holton, K.F. (2021). Brain concentrations of glutamate and GABA in human epilepsy: A review. Seizure *91*, 213–227. https://doi.org/10.1016/j.seizure.2021.06.028.

9. Umesawa, Y., Matsushima, K., Atsumi, T., Kato, T., Fukatsu, R., Wada, M., and Ide, M. (2020). Altered GABA Concentration in Brain Motor Area Is Associated with the Severity of Motor Disabilities in Individuals with Autism Spectrum Disorder. J. Autism Dev. Disord. *50*, 2710–2722. https://doi.org/10.1007/s10803-020-04382-x.

10. Porges, E.C., Woods, A.J., Edden, R.A.E., Puts, N.A.J., Harris, A.D., Chen, H., Garcia, A.M., Seider, T.R., Lamb, D.G., Williamson, J.B., and Cohen, R.A. (2017). Frontal Gamma-Aminobutyric Acid Concentrations Are Associated With Cognitive Performance in Older Adults. Biol. Psychiatry. Cogn. Neurosci. Neuroimaging *2*, 38–44. https://doi.org/10.1016/j.bpsc.2016.06.004.

11. Carello-Collar, G., Bellaver, B., Ferreira, P.C.L., Ferrari-Souza, J.P., Ramos, V.G., Therriault, J., Tissot, C., De Bastiani, M.A., Soares, C., Pascoal, T.A., et al. (2023). The GABAergic system in Alzheimer's disease: a systematic review with meta-analysis. Mol. Psychiatry *28*, 5025–5036. https://doi.org/10.1038/s41380-023-02140-w.

12. Solas, M., Puerta, E., and Ramirez, M.J. (2015). Treatment Options in Alzheimer's Disease: The GABA Story. Curr. Pharm. Des. *21*, 4960–4971. https://doi.org/10.2174/1381612821666150914121149.

13. Jia, F., Yue, M., Chandra, D., Keramidas, A., Goldstein, P.A., Homanics, G.E., and Harrison, N.L. (2008). Taurine is a potent activator of extrasynaptic GABA(A) receptors in the thalamus. J. Neurosci. *28*, 106–115. https://doi.org/10.1523/JNEUROSCI.3996-07.2008.

14. Ochoa-de la Paz, L., Zenteno, E., Gulias-Cañizo, R., and Quiroz-Mercado, H. (2019). Taurine and GABA neurotransmitter receptors, a relationship with therapeutic potential? Expert Rev. Neurother. *19*, 289–291. https://doi.org/10.1080/14737175.2019.1593827.

15. Alom, J., Mahy, J.N., Brandi, N., and Tolosa, E. (1991). Cerebrospinal fluid taurine in Alzheimer's disease. Ann. Neurol. *30*, 735. https://doi.org/10.1002/ana.410300518.

16. Aytan, N., Choi, J.K., Carreras, I., Brinkmann, V., Kowall, N.W., Jenkins, B.G., and Dedeoglu, A. (2016). Fingolimod modulates multiple neuroinflammatory markers in a mouse model of Alzheimer's disease. Sci. Rep. *6*, 24939. https://doi.org/10.1038/srep24939.

17. Chiquita, S., Ribeiro, M., Castelhano, J., Oliveira, F., Sereno, J., Batista, M., Abrunhosa, A., Rodrigues-Neves, A.C., Carecho, R., Baptista, F., et al. (2019). A longitudinal multimodal in vivo molecular imaging study of the 3xTg-AD mouse model shows progressive early hippocampal and taurine loss. Hum. Mol. Genet. *28*, 2174–2188. https://doi.org/10.1093/hmg/ddz045.

18. Garcia-Serrano, A.M., Vieira, J.P.P., Fleischhart, V., and Duarte, J.M.N. (2023). Taurine and N-acetylcysteine treatments prevent memory impairment and metabolite profile alterations in the hippocampus of high-fat diet-fed female mice. Nutr. Neurosci. *26*, 1090–1102. https://doi.org/10.1080/1028415X.2022.2131062.

19. Pomara, N., Singh, R., Deptula, D., Chou, J.C., Schwartz, M.B., and LeWitt, P.A. (1992). Glutamate and other CSF amino acids in Alzheimer's disease. Am. J. Psychiatry *149*, 251–254. https://doi.org/10.1176/ajp.149.2.251.

20. Vermeiren, Y., Le Bastard, N., Van Hemelrijck, A., Drinkenburg, W.H., Engelborghs, S., and De Deyn, P.P. (2013). Behavioral correlates of cerebrospinal fluid amino acid and biogenic amine neurotransmitter alterations in dementia. Alzheimers Dement. *9*, 488–498. https://doi.org/10.1016/j.jalz.2012.06.010.

21. Csernansky, J.G., Bardgett, M.E., Sheline, Y.I., Morris, J.C., and Olney, J.W. (1996). CSF excitatory amino acids and severity of illness in Alzheimer's disease. Neurology *46*, 1715–1720. https://doi.org/10.1212/wnl.46.6.1715.

22. Gao, R., Bae, M.A., Chang, K.J., and Kim, S.H. (2017). Comparison of Urinary Excretion of Taurine Between Elderly with Dementia and Normal Elderly. Adv. Exp. Med. Biol. *975*, 57–65. https://doi.org/10.1007/978-94-024-1079-2_5.

23. Fujii, Y., Nguyen, T.T.T., Fujimura, Y., Kameya, N., Nakamura, S., Arakawa, K., and Morita, H. (2019). Fecal metabolite of a gnotobiotic mouse transplanted with gut microbiota from a patient with Alzheimer's disease. Biosci. Biotechnol. Biochem. *83*, 2144–2152. https://doi.org/10.1080/09168451.2019.1644149.

24. Jang, H., Lee, S., Choi, S.L., Kim, H.Y., Baek, S., and Kim, Y. (2017). Taurine Directly Binds to Oligomeric Amyloid-beta and Recovers Cognitive Deficits in Alzheimer Model Mice. Adv. Exp. Med. Biol. *975*, 233–241. https://doi.org/10.1007/978-94-024-1079-2_21.

25. Kim, H.Y., Kim, H.V., Yoon, J.H., Kang, B.R., Cho, S.M., Lee, S., Kim, J.Y., Kim, J.W., Cho, Y., Woo, J., and Kim, Y. (2014). Taurine in drinking water recovers learning and memory in the adult APP/PS1 mouse model of Alzheimer's disease. Sci. Rep. *4*, 7467. https://doi.org/10.1038/srep07467.

26. Manzano, S., Agüera, L., Aguilar, M., and Olazarán, J. (2020). A Review on Tramiprosate (Homotaurine) in Alzheimer's Disease and Other Neurocognitive Disorders. Front. Neurol. *11*, 614. https://doi.org/10.3389/fneur.2020.00614.

27. Singh, P., Gollapalli, K., Mangiola, S., Schranner, D., Yusuf, M.A., Chamoli, M., Shi, S.L., Lopes Bastos, B., Nair, T., Riermeier, A., et al. (2023). Taurine deficiency as a driver of aging. Science *380*, eabn9257. https://doi.org/10.1126/science.abn9257.

28. Borsom, E.M., Lee, K., and Cope, E.K. (2020). Do the Bugs in Your Gut Eat Your Memories? Relationship between Gut Microbiota and Alzheimer's Disease. Brain Sci. *10*, 814. https://doi.org/10.3390/brainsci10110814.

29. Saji, N., Niida, S., Murotani, K., Hisada, T., Tsuduki, T., Sugimoto, T., Kimura, A., Toba, K., and Sakurai, T. (2019). Analysis of the relationship between the gut microbiome and dementia: a cross-sectional study conducted in Japan. Sci. Rep. *9*, 1008. https://doi.org/10.1038/s41598-018-38218-7.

30. Zhuang, Z.-Q., Shen, L.-L., Li, W.-W., Fu, X., Zeng, F., Gui, L., Lü, Y., Cai, M., Zhu, C., Tan, Y.-L., et al. (2018). Gut Microbiota is Altered in Patients with Alzheimer's Disease. J. Alzheimers Dis. *63*, 1337–1346. https://doi.org/10.3233/JAD-180176.

31. Guo, M., Peng, J., Huang, X., Xiao, L., Huang, F., and Zuo, Z. (2021). Gut Microbiome Features of Chinese Patients Newly Diagnosed with Alzheimer's Disease or Mild Cognitive Impairment. J. Alzheimers Dis. *80*, 299–310. https://doi.org/10.3233/JAD-201040.

32. Li, B., He, Y., Ma, J., Huang, P., Du, J., Cao, L., Wang, Y., Xiao, Q., Tang, H., and Chen, S. (2019). Mild cognitive impairment has similar alterations as Alzheimer's disease in gut microbiota. Alzheimers Dement. *15*, 1357–1366. https://doi.org/10.1016/j.jalz.2019.07.002.

33. Jemimah, S., Chabib, C.M.M., Hadjileontiadis, L., and AlShehhi, A. (2023). Gut microbiome dysbiosis in Alzheimer's disease and mild cognitive impairment: A systematic review and meta-analysis. PLoS One *18*, e0285346. https://doi.org/10.1371/journal.pone.0285346.

34. Salyers, A.A. (1984). Bacteroides of the human lower intestinal tract. Annu. Rev. Microbiol. *38*, 293–313. https://doi.org/10.1146/annurev.mi.38.100184.001453.

35. Wexler, H.M. (2007). Bacteroides: the good, the bad, and the nitty-gritty. Clin. Microbiol. Rev. *20*, 593–621. https://doi.org/10.1128/CMR.00008-07.

36. Strandwitz, P., Kim, K.H., Terekhova, D., Liu, J.K., Sharma, A., Levering, J., McDonald, D., Dietrich, D., Ramadhar, T.R., Lekbua, A., et al. (2019). GABA-modulating bacteria of the human gut microbiota. Nat. Microbiol. *4*, 396–403. https://doi.org/10.1038/s41564-018-0307-3.

37. Otaru, N., Ye, K., Mujezinovic, D., Berchtold, L., Constancias, F., Cornejo, F.A., Krzystek, A., de Wouters, T., Braegger, C., Lacroix, C., and Pugin, B. (2021). GABA Production by Human Intestinal Bacteroides spp.: Prevalence, Regulation, and Role in Acid Stress Tolerance. Front. Microbiol. *12*, 656895. https://doi.org/10.3389/fmicb.2021.656895.

38. Horvath, T.D., Ihekweazu, F.D., Haidacher, S.J., Ruan, W., Engevik, K.A., Fultz, R., Hoch, K.M., Luna, R.A., Oezguen, N., Spinler, J.K., et al. (2022). Bacteroides ovatus colonization influences the abundance of intestinal short chain fatty acids and neurotransmitters. iScience *25*, 104158. https://doi.org/10.1016/j.isci.2022.104158.

39. Capitani, G., De Biase, D., Aurizi, C., Gut, H., Bossa, F., and Grütter, M.G. (2003). Crystal structure and functional analysis of *Escherichia coli* glutamate decarboxylase. EMBO J. *22*, 4027–4037. https://doi.org/10.1093/emboj/cdg403.

40. Dutyshev, D.I., Darii, E.L., Fomenkova, N.P., Pechik, I.V., Polyakov, K.M., Nikonov, S.V., Andreeva, N.S., and Sukhareva, B.S. (2005). Structure of *Escherichia coli* glutamate decarboxylase (GADα) in complex with glutarate at 2.05 Å resolution. Acta Crystallogr. D Biol. Crystallogr. *61*, 230–235. https://doi.org/10.1107/S0907444904032147.

41. Chang, C., Zhang, J., Ma, S., Wang, L., Wang, D., Zhang, J., and Gao, Q. (2017). Purification and characterization of glutamate decarboxylase from Enterococcus raffinosus TCCC11660. J. Ind. Microbiol. Biotechnol. *44*, 817–824. https://doi.org/10.1007/s10295-017-1906-3.

42. Liu, S., Wen, B., Du, G., Wang, Y., Ma, X., Yu, H., Zhang, J., Fan, S., Zhou, H., and Xin, F. (2023). Coordinated regulation of Bacteroides thetaiotaomicron glutamate decarboxylase activity by multiple elements under different pH. Food Chem. *403*, 134436. https://doi.org/10.1016/j.foodchem.2022.134436.

43. Komatsuzaki, N., Nakamura, T., Kimura, T., and Shima, J. (2008). Characterization of glutamate decarboxylase from a high gamma-aminobutyric

acid (GABA)-producer, Lactobacillus paracasei. Biosci. Biotechnol. Biochem. *72*, 278–285. https://doi.org/10.1271/bbb.70163.

44. Hiraga, K., Ueno, Y., and Oda, K. (2008). Glutamate decarboxylase from Lactobacillus brevis: activation by ammonium sulfate. Biosci. Biotechnol. Biochem. *72*, 1299–1306. https://doi.org/10.1271/bbb.70782.
45. Giovannercole, F., Mérigoux, C., Zamparelli, C., Verzili, D., Grassini, G., Buckle, M., Vachette, P., and De Biase, D. (2017). On the effect of alkaline pH and cofactor availability in the conformational and oligomeric state of Escherichia coli glutamate decarboxylase. Protein Eng. Des. Sel. *30*, 235–244. https://doi.org/10.1093/protein/gzw076.
46. Beattie, A.E., Gupta, S.D., Frankova, L., Kazlauskaite, A., Harmon, J.M., Dunn, T.M., and Campopiano, D.J. (2013). The Pyridoxal 5′-Phosphate (PLP)-Dependent Enzyme Serine Palmitoyltransferase (SPT): Effects of the Small Subunits and Insights from Bacterial Mimics of Human hLCB2a HSAN1 Mutations. BioMed Res. Int. 194371. https://doi.org/10.1155/2013/194371.
47. Moore, P.S., Dominici, P., and Borri Voltattorni, C. (1996). Cloning and expression of pig kidney dopa decarboxylase: comparison of the naturally occurring and recombinant enzymes. Biochem. J. *315*, 249–256. https://doi.org/10.1042/bj3150249.
48. Zhou, X., and Toney, M.D. (1999). pH Studies on the Mechanism of the Pyridoxal Phosphate-Dependent Dialkylglycine Decarboxylase. Biochemistry *38*, 311–320. https://doi.org/10.1021/bi981455s.
49. Tramonti, A., John, R.A., Bossa, F., and De Biase, D. (2002). Contribution of Lys276 to the conformational flexibility of the active site of glutamate decarboxylase from *Escherichia coli*: Role of Lys276 in *E. coli* glutamate decarboxylase. Eur. J. Biochem. *269*, 4913–4920. https://doi.org/10.1046/j.1432-1033.2002.03149.x.
50. Pennacchietti, E., Lammens, T.M., Capitani, G., Franssen, M.C.R., John, R.A., Bossa, F., and De Biase, D. (2009). Mutation of His465 Alters the pH-dependent Spectroscopic Properties of Escherichia coli Glutamate Decarboxylase and Broadens the Range of Its Activity toward More Alkaline pH. J. Biol. Chem. *284*, 31587–31596. https://doi.org/10.1074/jbc.M109.049577.
51. Shukuya, R., and Schwert, G.W. (1960). Glutamic acid decarboxylase. II. The spectrum of the enzyme. J. Biol. Chem. *235*, 1653–1657.
52. Ueno, Y., Hayakawa, K., Takahashi, S., and Oda, K. (1997). Purification and characterization of glutamate decarboxylase from Lactobacillus brevis IFO 12005. Biosci. Biotechnol. Biochem. *61*, 1168–1171. https://doi.org/10.1271/bbb.61.1168.
53. Lee, C.Y., Liu, Y.L., Lin, C.L., Liu, G.Y., and Hung, H.C. (2014). Functional roles of the dimer-interface residues in human ornithine decarboxylase. PLoS One *9*, e104865. https://doi.org/10.1371/journal.pone.0104865.
54. Recsei, P.A., and Snell, E.E. (1970). Histidine decarboxylase of Lactobacillus 30a. VI. Mechanism of action and kinetic properties. Biochemistry *9*, 1492–1497. https://doi.org/10.1021/bi00809a003.
55. De Biase, D., and Pennacchietti, E. (2012). Glutamate decarboxylase-dependent acid resistance in orally acquired bacteria: function, distribution and biomedical implications of the gadBC operon. Mol. Microbiol. *86*, 770–786. https://doi.org/10.1111/mmi.12020.
56. Lee, J.Y., and Jeon, S.J. (2014). Characterization and immobilization on nickel-chelated Sepharose of a glutamate decarboxylase A from Lactobacillus brevis BH2 and its application for production of GABA. Biosci. Biotechnol. Biochem. *78*, 1656–1661. https://doi.org/10.1080/09168451.2014.936347.
57. Nomura, M., Nakajima, I., Fujita, Y., Kobayashi, M., Kimoto, H., Suzuki, I., and Aso, H. (1999). Lactococcus lactis contains only one glutamate decarboxylase gene. Microbiology (Read.) *145*, 1375–1380. https://doi.org/10.1099/13500872-145-6-1375.
58. Fonda, M.L. (1972). Glutamate decarboxylase. Substrate specificity and inhibition by carboxylic acids. Biochemistry *11*, 1304–1309. https://doi.org/10.1021/bi00757a029.
59. Fonda, M.L. (1985). L-Glutamate decarboxylase from bacteria. Methods Enzymol. *113*, 11–16. https://doi.org/10.1016/s0076-6879(85)13005-3.
60. Daniela De Biase, F.C., Pennacchietti, E., Giovannercole, F., Coluccia, A., Vepsäläinen, J., and Khomutov, A. (2020). Enzymatic kinetic resolution of desmethylphosphinothricin indicates that phosphinic group is a bioisostere of carboxyl group. Commn. Chem. *3*, 121.
61. Kim, H.W., Kashima, Y., Ishikawa, K., and Yamano, N. (2009). Purification and characterization of the first archaeal glutamate decarboxylase from Pyrococcus horikoshii. Biosci. Biotechnol. Biochem. *73*, 224–227. https://doi.org/10.1271/bbb.80583.
62. Tomita, H., Yokooji, Y., Ishibashi, T., Imanaka, T., and Atomi, H. (2014). An archaeal glutamate decarboxylase homolog functions as an aspartate decarboxylase and is involved in beta-alanine and coenzyme A biosynthesis. J. Bacteriol. *196*, 1222–1230. https://doi.org/10.1128/JB.01327-13.
63. Liu, P., Ge, X., Ding, H., Jiang, H., Christensen, B.M., and Li, J. (2012). Role of glutamate decarboxylase-like protein 1 (GADL1) in taurine biosynthesis. J. Biol. Chem. *287*, 40898–40906. https://doi.org/10.1074/jbc.M112.393728.
64. Richardson, G., Ding, H., Rocheleau, T., Mayhew, G., Reddy, E., Han, Q., Christensen, B.M., and Li, J. (2010). An examination of aspartate decarboxylase and glutamate decarboxylase activity in mosquitoes. Mol. Biol. Rep. *37*, 3199–3205. https://doi.org/10.1007/s11033-009-9902-y.
65. Wu, J.Y. (1982). Purification and characterization of cysteic acid and cysteine sulfinic acid decarboxylase and L-glutamate decarboxylase from bovine brain. Proc. Natl. Acad. Sci. USA *79*, 4270–4274. https://doi.org/10.1073/pnas.79.14.4270.
66. Blindermann, J.M., Maitre, M., Ossola, L., and Mandel, P. (1978). Purification and some properties of L-glutamate decarboxylase from human brain. Eur. J. Biochem. *86*, 143–152. https://doi.org/10.1111/j.1432-1033.1978.tb12293.x.
67. Agnello, G., Chang, L.L., Lamb, C.M., Georgiou, G., and Stone, E.M. (2013). Discovery of a Substrate Selectivity Motif in Amino Acid Decarboxylases Unveils a Taurine Biosynthesis Pathway in Prokaryotes. ACS Chem. Biol. *8*, 2264–2271. https://doi.org/10.1021/cb400335k.
68. Winge, I., Teigen, K., Fossbakk, A., Mahootchi, E., Kleppe, R., Sköldberg, F., Kämpe, O., and Haavik, J. (2015). Mammalian CSAD and GADL1 have distinct biochemical properties and patterns of brain expression. Neurochem. Int. *90*, 173–184. https://doi.org/10.1016/j.neuint.2015.08.013.
69. Mahootchi, E., Cannon Homaei, S., Kleppe, R., Winge, I., Hegvik, T.A., Megias-Perez, R., Totland, C., Mogavero, F., Baumann, A., Glennon, J.C., et al. (2020). GADL1 is a multifunctional decarboxylase with tissue-specific roles in beta-alanine and carnosine production. Sci. Adv. *6*, eabb3713. https://doi.org/10.1126/sciadv.abb3713.
70. Boldyrev, A.A., Aldini, G., and Derave, W. (2013). Physiology and pathophysiology of carnosine. Physiol. Rev. *93*, 1803–1845. https://doi.org/10.1152/physrev.00039.2012.
71. Sale, C., Saunders, B., and Harris, R.C. (2010). Effect of beta-alanine supplementation on muscle carnosine concentrations and exercise performance. Amino Acids *39*, 321–333. https://doi.org/10.1007/s00726-009-0443-4.
72. Lopez-Samano, M., Beltran, L.F.L., Sanchez-Thomas, R., Davalos, A., Villasenor, T., Garcia-Garcia, J.D., and Garcia-de Los Santos, A. (2020). A novel way to synthesize pantothenate in bacteria involves beta-alanine synthase present in uracil degradation pathway. Microbiologyopen *9*, e1006. https://doi.org/10.1002/mbo3.1006.
73. Hata, J., Ohara, T., Katakura, Y., Shimizu, K., Yamashita, S., Yoshida, D., Honda, T., Hirakawa, Y., Shibata, M., Sakata, S., et al. (2019). Association Between Serum beta-Alanine and Risk of Dementia. Am. J. Epidemiol. *188*, 1637–1645. https://doi.org/10.1093/aje/kwz116.
74. Ostfeld, I., Ben-Zeev, T., Zamir, A., Levi, C., Gepner, Y., Springer, S., and Hoffman, J.R. (2023). Role of β-Alanine Supplementation on Cognitive Function, Mood, and Physical Function in Older Adults; Double-Blind

Randomized Controlled Study. Nutrients *15*, 923. https://doi.org/10.3390/nu15040923.

75. Parle, M., Kulkarni, S., and Dhingra, D. (2006). β - Alanine protects mice from memory deficits induced by ageing, scopolamine, diazepam and ethanol. Indian J. Pharm. Sci. *68*, 216. https://doi.org/10.4103/0250-474X.25718.
76. Wu, J.-Y., Matsuda, T., and Roberts, E. (1973). Purification and Characterization of Glutamate Decarboxylase from Mouse Brain. J. Biol. Chem. *248*, 3029–3034. https://doi.org/10.1016/S0021-9258(19)44004-0.
77. Jumper, J., Evans, R., Pritzel, A., Green, T., Figurnov, M., Ronneberger, O., Tunyasuvunakool, K., Bates, R., Žídek, A., Potapenko, A., et al. (2021). Highly accurate protein structure prediction with AlphaFold. Nature *596*, 583–589. https://doi.org/10.1038/s41586-021-03819-2.
78. Miller, M.A., Pfeiffer, W., and Schwartz, T. (2010). Creating the CIPRES Science Gateway for Inference of Large Phylogenetic Trees. In Proceedings of the Gateway Computing Environments Workshop (GCE), (New Orleans, LA) pp. 1–8. https://doi.org/10.1109/GCE.2010.5676129.
79. Katoh, K., Misawa, K., Kuma, K.i., and Miyata, T. (2002). MAFFT: a novel method for rapid multiple sequence alignment based on fast Fourier transform. Nucleic Acids Res. *30*, 3059–3066. https://doi.org/10.1093/nar/gkf436.
80. Letunic, I., and Bork, P. (2021). Interactive Tree Of Life (iTOL) v5: an online tool for phylogenetic tree display and annotation. Nucleic Acids Res. *49*, W293–W296. https://doi.org/10.1093/nar/gkab301.
81. Price, M.N., Dehal, P.S., and Arkin, A.P. (2009). FastTree: computing large minimum evolution trees with profiles instead of a distance matrix. Mol. Biol. Evol. *26*, 1641–1650. https://doi.org/10.1093/molbev/msp077.
82. Price, M.N., Dehal, P.S., and Arkin, A.P. (2010). FastTree 2--approximately maximum-likelihood trees for large alignments. PLoS One *5*, e9490. https://doi.org/10.1371/journal.pone.0009490.
83. Cozzani, I. (1970). Spectrophotometric assay of l-glutamic acid decarboxylase. Anal. Biochem. *33*, 125–131. https://doi.org/10.1016/0003-2697(70)90446-X.
84. Tramonti, A., De Biase, D., Giartosio, A., Bossa, F., and John, R.A. (1998). The roles of His-167 and His-275 in the reaction catalyzed by glutamate decarboxylase from Escherichia coli. J. Biol. Chem. *273*, 1939–1945. https://doi.org/10.1074/jbc.273.4.1939.
85. Tsukatani, T., Higuchi, T., and Matsumoto, K. (2005). Enzyme-based microtiter plate assay for γ-aminobutyric acid: Application to the screening of γ-aminobutyric acid-producing lactic acid bacteria. Anal. Chim. Acta *540*, 293–297. https://doi.org/10.1016/j.aca.2005.03.056.
86. De Biase, D., Tramonti, A., John, R.A., and Bossa, F. (1996). Isolation, overexpression, and biochemical characterization of the two isoforms of glutamic acid decarboxylase from Escherichia coli. Protein Expr. Purif. *8*, 430–438. https://doi.org/10.1006/prep.1996.0121.
87. Tramonti, A., Contestabile, R., Florio, R., Nardella, C., Barile, A., and Di Salvo, M.L. (2021). A Novel, Easy Assay Method for Human Cysteine Sulfinic Acid Decarboxylase. Life *11*, 438. https://doi.org/10.3390/life11050438.
88. Goujon, M., McWilliam, H., Li, W., Valentin, F., Squizzato, S., Paern, J., and Lopez, R. (2010). A new bioinformatics analysis tools framework at EMBL-EBI. Nucleic Acids Res. *38*, W695–W699. https://doi.org/10.1093/nar/gkq313.
89. Sievers, F., Wilm, A., Dineen, D., Gibson, T.J., Karplus, K., Li, W., Lopez, R., McWilliam, H., Remmert, M., Söding, J., et al. (2011). Fast, scalable generation of high-quality protein multiple sequence alignments using Clustal Omega. Mol. Syst. Biol. *7*, 539. https://doi.org/10.1038/msb.2011.75.

STAR★METHODS

KEY RESOURCES TABLE

REAGENT or RESOURCE	SOURCE	IDENTIFIER
Bacterial and virus strains		
E. coli BL21(DE3)	New England Biolabs	C2527H
E. coli NEB5α	New England Biolabs	C2987H
pET28a	Lab stock	
Chemicals, peptides, and recombinant proteins		
kanamycin	Sigma-Aldrich	Cat#K1377
GABase	Sigma-Aldrich	Cat#G7509
β-ME	Sigma-Aldrich	Cat#1610710
α-ketoglutarate	Sigma-Aldrich	Cat#K1128
D-glutamic acid	Sigma-Aldrich	Cat#G1001
L-cysteine sulfinic acid monohydrate	Sigma-Aldrich	Cat#270881
L-cysteic acid monohydrate	Sigma-Aldrich	Cat#30170
GABA	Sigma-Aldrich	Cat#A5835
Hypotaurine	Sigma-Aldrich	Cat#H1384
Taurine	Sigma-Aldrich	Cat#T0625
Homotaurine	Sigma-Aldrich	Cat#A76109
L- Homocysteic acid	Sigma-Aldrich	Cat#H9633
L-aspartic acid sodium salt	Sigma-Aldrich	Cat#A6683
β-alanine	Sigma-Aldrich	Cat#146064
HEPES	Sigma-Aldrich	Cat#H3375
Imidazole	Sigma-Aldrich	Cat#I2399
pyridoxal5'-phosphate monohydrate	Sigma-Aldrich	Cat#82870
TLC Silica gel 60 F_{254}	Sigma-Aldrich	Cat#1.05721
Sodium L- glutamate monohydrate	Fisher Scientific	Cat#G0188
Luria-Bertani Broth (LB)	Fisher Scientific	Cat#BP14262
Sodium chloride	Fisher Scientific	Cat#S271
$NADP^+$ disodium salt	Fisher Scientific	Cat#481972
Sodium acetate	Fisher Scientific	Cat#S210
IPTG	Fisher Scientific	Cat#AM9462
ninhydrin	Fisher Scientific	Cat#A10409.18
Acetone	Fisher Scientific	Cat#67-64-1
Tris-HCL	Fisher Scientific	Cat#H5121
NdeI	New England Biolabs	Cat#R0111S
HindIII	New England Biolabs	Cat#R3104S
BfGAD_{WT}	This study	
BfGAD_{F81W}	This study	
BfGAD_{D104N}	This study	
Recombinant DNA		
pET28a-*Bf*GAD	This study	
pET28a-*Bf*GAD_{D104N}	This study	
pET28a-*Bf*GAD_{F81W}	This study	
Software and algorithms		
Code needed for TLC image analysis	This study	Zenodo: https://zenodo.org/records/14962663 GitHub: https://github.com/Pavani-dadi/TLC_profile

(*Continued on next page*)

Continued

REAGENT or RESOURCE	SOURCE	IDENTIFIER
Alphafold2	Jumper[77]	https://alphafold.com/
PyMOL	Schrodinger	https://pymol.org/
CIPRES	Miller[78]	https://www.phylo.org/
MAFFT in CIPRES	Katoh[79]	https://www.phylo.org/tools/mafft_xsede.html
iTOL	Letunic[80]	https://itol.embl.de/
FastTreeMP in CIPRES	Price[81,82]	https://www.phylo.org/tools/fasttree_xsede.html

EXPERIMENTAL MODEL AND STUDY PARTICIPANT DETAILS

The bacterial strains used in this study are listed in the key resources table. Two primary *Escherichia coli* strains were used: NEB5α for cloning and BL21(DE3) for protein overexpression. Both strains were stored at –80°C and cultivated at 37°C in Luria-Bertani (LB) medium supplemented with kanamycin at 50 μg/mL for plasmid selection.

METHOD DETAILS

Gene cloning

A synthesized gene for *B. fragilis* glutamate decarboxylase (*Bf*GAD) was created with the help of Genewiz from Azenta life sciences. The gene was codon optimized for expression in *E. coli* cells, which was then subcloned into a pET28a expression vector between the NdeI and HindIII restriction sites to incorporate an N-terminal hexahistidine (His_6) Tag. The pET28a-*Bf*GAD construct was confirmed by agarose gel electrophoresis, restriction digestion, sanger sequencing (Genewiz), and full plasmid sequencing (Plasmidsaurus) and then transformed into *E. coli* NEB5α and *E. coli* BL21(DE3) competent cells by heat shock. Glycerol stocks of the cells harboring the construct pET28a-*Bf*GAD were stored at –80°C.

Expression and purification of *Bf*GAD$_{WT}$ and engineered *Bf*GADs

E. coli BL21(DE3) cells containing the pET28a-*Bf*GADs were cultivated in LB medium containing kanamycin (50 μg/mL) with shaking (200 rpm) at 37°C until OD_{600} reached 0.7. At this point, the *Bf*GAD expression was induced with isopropyl β-D-1-thiogalactopyranoside (IPTG) to a final concentration of 1 mM and growth was continued at 37°C for 3 hours to allow for protein expression with continuous shaking at 200 rpm. Cells were harvested via centrifugation at 4000*g* for 30 min at 4°C and cell pellets were stored at –80°C. The frozen cell pellets were thawed on ice and resuspended in buffer A containing 20 mM Tris-HCl, 500 mM NaCl, 40 mM imidazole, 0.1 mM PLP, pH 7.8. All subsequent purification steps were carried out at 4°C. The cells were disrupted by sonication (20000 Hz for 10 cycles of 30 seconds each altering 1 minute on ice) and centrifuged at 13500*g* at 4°C for 30 min to separate supernatant from cell debris. The supernatant was then filtered through 0.2 μm PES filter membrane and loaded onto a HisTrap HP column (5 ml, 1.6 x 2.5 cm, Ni Sepharose High-performance column, GE Healthcare, now Cytiva) pre-equilibrated with buffer A at 1 mL/min. The wash step was carried out by running 5-column volumes of lysis buffer A to elute contaminating proteins. *Bf*GAD was eluted with a linear gradient from buffer A (containing 40 mM imidazole) to an elution buffer B containing 20 mM Tris-HCl, 500 mM NaCl, 400 mM imidazole, 0.1 mM PLP, pH 7.8 at 2 mL/min. Eluted protein peaks were pooled, buffer exchanged and concentrated to a final buffer (50 mM HEPES, pH 7.2) using Vivaspin 50 kDa MWCO filters (Cytiva). Aliquots of purified proteins were stored at –80°C. Engineered *Bf*GADs were purified similarly. SDS-PAGE analysis and activity assays were performed to confirm the purity and presence of functional *Bf*GAD proteins.

Gel filtration chromatography with *Bf*GAD$_{WT}$

To understand oligomeric state of *Bf*GAD$_{WT}$, gel filtration chromatography was performed at two different pH, 4.7 (50 mM sodium acetate, 150 mM NaCl) and pH 7.2 (50 mM HEPES, 150 mM NaCl), and in the presence of external PLP (overnight incubation of *Bf*GAD$_{WT}$ was carried out with 2 mM PLP before gel filtration chromatography) using HiPrep™ 16/60 Sephacryl® S-200 HR column. Equilibration and elution steps were carried out at a flow rate of 0.5 mL/min. High molecular weight (HMW) and Low molecular weight (LMW) calibration kits (Cytiva) were used for column calibration, to create a standard curve, and for molecular weight determination (Figures S6B and S6C).

Activity assays

*Bf*GAD activity assays were performed by a coupled enzyme assay with a GABase system to measure GABA production spectrophotometrically. Briefly, *Bf*GAD was incubated with 50 mM L-glutamate in 50 mM sodium acetate, pH 4.7 buffer or in buffers at other pH values for one hour at 25°C. Enzymatic reactions were stopped by boiling samples for 15 min. These samples were then

centrifuged at 6000*g* for 5 min and if necessary, dilutions were created in 50 mM Tris-HCl, pH 8.6. For GABA measurement, 75 μL of samples (either diluted or undiluted) were added to 25 μL of Gabase assay mix containing 10 mM BME, 2 mM α-ketoglutarate, 600 μM $NADP^+$, and 30 μg (0.015U/mL) of GABase in 50 mM Tris-HCl, pH 8.6.[49,83–86] In the GABase assay, GABA is converted to succinic semialdehyde (SSA) and then to succinate with subsequent production of NADPH which was measured at 340 nm. Using an extinction coefficient of 6,220 M^{-1} cm^{-1} at 340 nm, NADPH concentrations were calculated which will provide GABA concentrations in measured samples ([NADPH]=[GABA]). Activity assays with D-glutamate were carried out similarly.

*Bf*GAD absorbance spectrophotometry and activity assays with pH variation

Spectra of $BfGAD_{WT}$ were recorded from 200 nm - 800 nm in buffers at pH 4.7, 5.5, 6.7, 7.5, and 8.6 at 25°C on Agilent Cary 3500 UV-Vis spectrophotometer. From these spectra, absorbance changes at 335 nm (enolimine) and 420 nm (ketoenamine) for enzyme bound PLP cofactor were collected. A plot of pH versus absorbance at 420 nm was generated and the curve fitting was carried out using Equation 1.[39]

$$\frac{\mathrm{AbsHnE} - \mathrm{AbsE}}{\mathrm{Abs} - \mathrm{AbsE}} - 1 = \frac{\left[10^{-\mathrm{npK}}\right]}{\left[10^{-\mathrm{npH}}\right]} \quad \text{(Equation 1)}$$

Where pK is the acid dissociation constant, number of protons involved in the titration is n and, AbsHnE and AbsE are the absorbances at acidic and basic pH which produce protonated and deprotonated forms of the enzymes. The initial activity assays for the $BfGAD_{WT}$ were performed in buffers at pH 4.7 - 8 with GABase assay system as mentioned in the above method. Based on the results of these activity assays, all subsequent enzymatic assays were carried out at pH 4.7.

Steady-state kinetics

Kinetic parameters of $BfGAD_{WT}$ were determined by varying $BfGAD_{WT}$ concentrations (25 nM-100 nM) and by varying L-glutamate concentrations (0.125 mM-32 mM) in 50 mM sodium acetate, pH 4.7 at 25°C. For enzyme concentration variation experiments, reaction samples with each enzyme concentration were collected at 1 min time point after starting the reaction and then stopped by boiling for 15 min. Once cooled to room temperature, these samples were analyzed for GABA content with GABase assay as mentioned above. For the substrate concentration variation experiments, 100 μL aliquots of reactions with each substrate concentration were collected at different time intervals (0.2 – 30 min). The reactions were stopped by boiling the samples for 15 minutes. Once cooled to room temperature, these samples were analyzed for GABA content with GABase assay as mentioned above. The initial velocities of various reactions were calculated by fitting data of early timepoints to a linear regression. These initial velocities were then plotted against substrate concentrations and curve fitting was carried out using Equation 2.

$$v = \frac{V_{max}[S]^h}{(k_{half})^h + [S]^h} \quad \text{(Equation 2)}$$

Where v is the initial velocity, V_{max} is the maximum velocity, K_{half} is the concentration of substrate at which the reaction velocity is half of V_{max}, [S] is the substrate concentration, h is the hill coefficient.

Generation of engineered *Bf*GAD variants

The pET28a-*Bf*GAD was used as a template for the generation of engineered *Bf*GAD variants. $BfGAD_{D104N}$ and $BfGAD_{F81W}$ were created by site-directed mutagenesis with Phusion DNA polymerase using the following primer pairs incorporating codons for the specific amino acid substitution (bold).

For $BfGAD_{D104N}$

F: 5' CCGCAATGCGCGGATATTCGGTTTC**ATT**AATATAGTTAATG 3'
R: 5' CATTAACTATATT**AAT**GAAACCGAATATCCGCGCATTGCGG 3'

For $BfGAD_{F81W}$

F: 5' CATCCATATAGGTGGTCACCCAGGTCG**CCA**GGTTCAGGCGCG 3'
R: 5' CGCGCCTGAACCTGGCGACC**TGG**GTGACCACCTATATGGATG 3'

The variants were confirmed by gene sequencing (Genewiz) and full plasmid sequencing with Plasmidsaurus.

$CO_{2(g)}$ detection by headspace gas chromatography

All enzymatic reactions and controls were prepared in 6 mL vials and sealed prior to starting the reaction. The reactions were started by the addition of *Bf*GAD (WT or engineered variants) with a syringe into the reaction mixture containing 50 mM substrate in 50 mM sodium acetate, pH 4.7. These vials were incubated at 37°C for 24 hours and 48 hours. Headspace GC measurements were carried out on an Agilent 8890 gas chromatograph system equipped with a flame ionization detector (FID) and a Hayesep Q packed column (1.8 m x 2 mm x 3.17 mm) (Agilent) operating with an Argon carrier gas (flow rate= 5 mL/min). The oven was programmed to hold 30°C

for 6.5 min, ramp at 30°C/min to 280°C with a hold for 4 min for a total run time of 18.83 min. The flame ionization detector was used for the detection of CO_2 gas with a temperature setting of 275°C, hydrogen flow of 60 mL/min, air flow of 400 mL/min and constant makeup gas (nitrogen) at 5 mL/min. The retention time for CO_2 gas was 12.83 min. Multiple standards of CO_2 gas were analyzed by this method to confirm retention time before injecting reaction samples (Figure S16).

Thin layer chromatography (TLC)

Silica gel plates (stationary phase) with a solvent system (mobile phase) of 3:1:1 ratio of butanol: acetic acid: H_2O were used to separate reaction products from substrates.[87] 2 μL of reaction mixtures were spotted on glass silica plates along with 10 mM of various metabolites (L-glutamate, D-glutamate, L-CSA, L-CA, L-HCA, L-Aspartate, GABA, hypotaurine, taurine, homotaurine and β-alanine) as standards. Separation via TLC was carried out at 25°C for 3-4 hours in an above-mentioned mobile phase. Once mobile phase reached a sufficient height on the TLC plate, chromatographic separation was discontinued. Plates were treated with 0.5% ninhydrin in acetone (w/v) and heated minimally with a dryer for the color development. The TLC plate images were initially inverted via ImageJ and then intensity of each spot was quantified by a custom python code.

Liquid chromatography with tandem mass spectrometry (LC-MS/MS) detection of decarboxylated products from reactions catalyzed by *Bf*GADs (WT and engineered variants)

Samples were analyzed by ESI-LC-MS/MS in positive (products) and negative ion (substrates) mode using a Thermo vanquish LC and TSQ Altis Triple Quadrupole Mass Spectrometer. Samples were separated by gradient elution using Agilent Infinity lab Poroshell 120 HILIC-Z 2.1 x 100 mm, 2.7 μm column at 25°C with 20 mM ammonium formate, pH 3.0 (Solvent A) and 20 mM ammonium formate in 9:1 acetonitrile: H_2O, pH 3.0 (Solvent B). Elution was initiated at 70% B for 11.5 min, followed by gradient elution from 70 to 100% B over 11.5 min, and 100% B for 4 min at a flow rate of 0.5mL/min. The precursor to product transitions of *m/z* $[M+H]^-$152→ 88.1(Cysteine sulfinic acid), $[M+H]^-$ 168→ 81.1(Cysteic acid), $[M+H]^+$110.1→ 45.1(hypotaurine), $[M+H]^+$126.1→ 44.1(taurine) were employed to monitor substrates and products.

Multiple sequence alignment and phylogenetic analyses of gut microbial GADs

All the protein sequences were obtained from NCBI. Multiple sequence alignments were performed using Clustal Omega (1.2.4) tool with default parameters.[88,89] The phylogenetic trees were created for GADs using cyberinfrastructure for phylogenetic research (CIPRES).[78] Within CIPRES, the MAFFT on XSEDE (7.505)[79] was utilized to create a separate multiple sequence alignment that goes through FastTreeMP on XSEDE(2.1.10)[81,82] to obtain the phylogenetic tree files which can be visualized and annotated with Interactive tree of life (iTOL v6.8.1).[80]

*Bf*GAD dimer generation with the AlphaFold2 and visualization, structural alignments, and mutagenesis via PyMOL

The dimer structure of wildtype *Bf*GAD was generated using AlphaFold2[77] and visualized using PyMOL. Variants were then created using the mutagenesis wizard in PyMOL. Rotamers for the altered residues were selected based on their best fit to the position of wild-type residues in the *Bf*GAD protein. All structural alignments were carried out using PyMOL align method, involving five iteration cycles and a cutoff of 2 Å.

QUANTIFICATION AND STATISTICAL ANALYSIS

Statistical analysis was performed using GraphPad Prism. The specific statistical parameters are reported in the relevant figure legends. All data points on graphs represent the average of n experimental replicates, where n ranges from 2 to 4. Error bars on all graphs represent SD.